








	<h1>H2020</h1>		
			
			
<h1>PERIODIC TECHNICAL REPORT 3</h1>			
<p>FLAIR - FLying ultraA-broadband single-shot InfraRed Sensor <b>GA732968</b></p>			
<b>Deliverable Information</b>			
<b>Deliverable Number:</b> D1.9		<b>Work Package:</b> WP1	
<b>Date of Issue:</b> 05.12.2019			
<b>Document Reference:</b> 732968 D1.9 PeriodicTechnicalReport3			
<b>Version Number:</b> 2.1			
<b>Nature of Deliverable:</b> Report		<b>Dissemination Level of Deliverable:</b> PU	
<b>Author(s):</b> CSEM (Responsible), SA, NKT, NIT, RUN, EMPA, DTU			
<b>Keywords:</b> Technical report			
<b>Abstract:</b> This document constitutes the third periodic technical report for FLAIR and reports on the progress of the technical tasks foreseen in the DoA during the third year of the project (i.e. from November 2018 to October 2019).			

## Document History

Date	Version	Remarks
05/11/2019	0.1	Skeleton
22/11/2019	0.2	Merge of partner contributions
28/11/2019	0.3	Corrupted Word version
02/12/2019	1.0	Released by CSEM to RUN and partners for review
05/12/2019	2.0	Reviewed version ready for submission
05/12/2019	2.1	Minor polishing

## Document Authors

Entity	Contributors
CSEM	Laurent Balet Sanghoon Chin Fabian Lutolf
DTU	Getinet Woyessa Ole Bang
EMPA	Christoph Hüglin
NIT	Germán Vergara Ogando
NKT	Laurent Huot Patrick Bowen
RUN	Frans Harren Amir Khodabakhsh
SA	Hans Martin

**Disclosure Statement:** The information contained in this document is the property of FLAIR Consortium and it shall not be reproduced, disclosed, modified or communicated to any third parties without the prior written consent of the abovementioned entities.

## Executive Summary

The **FLAIR** project addresses the challenge of performing air quality monitoring in complex urban environments by mounting a high-performance air sampling sensor based on photonic technology on a drone for pervasive, high specificity and high sensitivity air quality sensing with large area coverage. Operating in the two atmospheric windows of  $3.7\text{ }\mu\text{m}$  and  $8.5\text{ }\mu\text{m}$  wavelength, **FLAIR** can detect minute traces of molecules in complex gas mixtures from their characteristic infrared (IR) absorption fingerprints and provide real time information to the operator of the drone. **FLAIR** can operate in remote or dangerous areas and outside of established monitoring networks.

This document constitutes the third periodic technical report for the project. Its purpose is to provide a summary of the activities performed during the third year of the project (i.e. from November 2018 to October 2019) and, in particular, to document the progress made towards the goals of the action, the problems encountered and the barriers overcome. Consistency with the predicted implementation path in the Description of Action (DoA) is assessed through an overview of the project's milestones, the status of deliverables and verification of expected impacts. Deviations from the predicted effort for each work package (WP) are also registered and sufficiently justified in this report.

## Table of Contents

Document History.....	2
Document Authors.....	2
Executive Summary .....	3
Table of Contents.....	4
List of Tables.....	4
List of Figures.....	5
List of Acronyms.....	7
1 Introduction.....	8
2 Approach.....	9
3 Project progress overview .....	9
4 Laboratory spectroscopy (WP3) results.....	9
4.1 Detection of a 1D dispersed beam on the camera.....	9
4.2 Recording the same 1D spectrum on different pixel arrays.....	12
4.3 Recording the same 1D spectrum with different bias voltages.....	13
4.4 Recording the same 1D spectrum with different integration times.....	14
4.5 2D spectrum of CH <sub>4</sub> .....	14
4.6 1D dispersed beam on the camera before and after NUC.....	16
4.7 The same 1D spectrum on different pixel arrays before and after NUC.....	18
4.8 Conclusions.....	20
5 Sensor subsystems development (WP4) results.....	21
5.1 Supercontinuum sources.....	21
5.1.1 2-5 $\mu\text{m}$ source.....	21
5.1.2 8-12 $\mu\text{m}$ source.....	25
5.2 Multipass cell.....	27
5.3 Gas Handling System.....	29
5.3.1 Multipass cell gas handling system.....	29
5.3.2 Laboratory gas handling system.....	30
5.4 2D spectrometer and imaging optics.....	32
5.4.1 Laboratory setup.....	32
5.4.2 Consortium decision.....	44
5.4.3 UAV compatible setup.....	45
5.5 PbSe Camera.....	48
5.6 Data processing algorithm.....	50
5.7 Control electronics.....	51
5.7.1 Control interface.....	52
5.7.2 Power distribution board.....	52
6 Airborne platform adaptation and sensor integration (WP5).....	53
7 Validation and demonstration (WP6) .....	53
8 Other .....	54
8.1 Dissemination.....	54

## List of Tables

Table 1: List of acronyms. ....	7
Table 2 : Long-pass filtered measurements of the laser's output power. ....	22
Table 3 : CH <sub>4</sub> concentration by combining two gas bottles.....	31
Table 4 : List of the powered equipment, with nominal voltage and power consumption.....	52

## List of Figures

Figure 1 : The stripe from the diffracted broadband light on the camera .....	10
Figure 2 : (a) The recorded spectra for 10 consecutive camera measurements. (b) The recorded dark noise for 10 consecutive camera measurements. The details of the measurements are explained in the text. ....	11
Figure 3 : (a) The recorded spectra for 10 consecutive, 1000 averages camera measurements. (b) The recorded dark noise for 10 consecutive, 1000 averages camera measurements. The details of the measurements are explained in the text. (c) A zoom around pixels #11 .....	11
Figure 4 : (a) to (c) The stripe from the diffracted broadband light on the camera measured at three different beam high with three different rows of pixels. (d) to (f) the corresponding measured spectra from (a) to (b) images respectively. ....	13
Figure 5 : The same 1D spectrum measured with three different rows of the camera.....	13
Figure 6 : (a) The same 1D spectrum measured with three different camera bias voltages (blue curve 1.50 V, red curve 1.75 V, and yellow curve 2.00 V). (b) The normalized spectra measured in (a).....	14
Figure 7 : The same 1D spectrum measured with two different camera integration times (blue curve 200 $\mu$ s and red 100 $\mu$ s). (b) The normalized spectra measured in (a). ....	14
Figure 8 : Measured (a) background (lab air sample) cand (b) signal (100% CH <sub>4</sub> sample) image spectra, as well as the same corresponding spectra for background and signal after removing the image skew in (c) and (d) respectively.....	15
Figure 9 : (a) single shot measurement of the signal (in red) and background (in blue). (b) the subtraction of the signal and background. ....	16
Figure 10 : (a) 1000 average measurement of the signal (in red) and background (in blue). (b) the subtraction of the signal and background. ....	16
Figure 11 : The stripe from the diffracted broadband light on the camera. ....	16
Figure 12 : (a) The recorded spectra for 20 camera measurements. (b) The recorded dark noise for 20 camera measurements. (c) The averaged spectrum and (d) the averaged dark noise. The details of the measurements are explained in the text.....	17
Figure 13 : (a) The recorded spectra for 20 consecutive measurements. (b) The recorded dark noise for 20 consecutive measurements. The details of the measurements are explained in the text. (c) The average spectrum and (d) the average dark noise.....	18
Figure 14 : (a) to (c) The stripe from the diffracted broadband light on the camera measured at three different beam high with three different rows of pixels (averaged 20 times). (d) to (f) depicts the corresponding measured spectra from (a) to (c) images, respectively, before NUC and (g) to (i) shows the same spectra after NUC. ....	19
Figure 15 : The same 1D spectrum measured with three different rows of the camera as the previous figure (in different colors) in (a) before NUC and (b) after NUC. (c) and (d) depict the dark noise of each different row before and after NUC, respectively.....	20
Figure 16 : Packaging of the super continuum source showing compact 220x150x55 mm dimensions and output armoured cable with collimating Thorlabs fiber port on the output....	22
Figure 17 : Power variation of the supercontinuum source measured over a 16h period. ....	23
Figure 18 : Output spectrum of the optimised laser system. ....	23
Figure 19 : Output spectrum of the previous laser system. ....	24
Figure 20 : Focusing fiber port (left) and stainless-steel ferrules (right).....	24
Figure 21 : FLAIR LW-MIR SC architecture.....	25
Figure 22 : Measured output spectrum of the FLAIR 1.72-10 $\mu$ m supercontinuum source....	26
Figure 23 : Packaged LW-MIR FLAIR supercontinuum source in a 474 x 300 x 134.5mm box. ....	26
Figure 24 : The multipass cell with thermos system (right), and sub systems (left). ....	27

Figure 25 : The multipass cell thermos with two fans (on upper half) for inner closed space air circulation, and heater with thermistor (on lower part) for thermos temperature regulation. ...	28
Figure 26 : The multipass cell system control block diagram. ....	28
Figure 27 : Location of T/P/RH sensors in the inner optics chamber (BME280).....	29
Figure 28 : The current multipass cell prototype with fan, and control card connected with wires. ....	29
Figure 29 : Gas handling system for the test proto-MPC, using a vacuum pump.....	30
Figure 30 : Gas handling system for the test proto-MPC, using a fan.....	30
Figure 31 : Schematic diagram of controlling the CH <sub>4</sub> concentration inside the gas cell.....	31
Figure 32 : Experimental setup of controlling the CH <sub>4</sub> concentration inside the gas cell.....	32
Figure 33 : VIPA based 2D spectrometer setup. (top) sketch (bottom) laboratory realization. ....	33
Figure 34 : Comparison between HITRAN simulated absorption spectrum (top, green) and actual measurement on N <sub>2</sub> O reference cell (bottom, red) indicate a spectral coverage of 35.1 cm <sup>-1</sup> and spectral resolution of 0.1 cm <sup>-1</sup> . ....	34
Figure 35 : (left) example 2D absorption spectrum of N <sub>2</sub> O recorded on the NIT camera, and (left) linearization of the 2D spectrum line by line, with each line shown in different color for clarity.....	35
Figure 36 : Sketch illustrating the working principle of the crossed-grating 2D spectrometer. ....	35
Figure 37 : Zemax model used to validate the sketched concept.....	36
Figure 38 : Experimental setup of 2D spectroscopy, using a combination of one echelle grating and one normal grating.....	36
Figure 39 : Measured CH <sub>4</sub> concentration at 40000ppm in a 10cm long cell, using echelle grating-based spectroscopy.....	37
Figure 40 : CH <sub>4</sub> absorption profiles and the repeatability for different gas concentrations. ...	38
Figure 41 : (top) schematic principle of a prism used for cross-dispersion of the absorption spectrum. (Bottom) Zemax model to evaluate the possibility to use a prism for the cross dispersion.....	38
Figure 42 : Single grating-based spectrometer. ....	39
Figure 43 : Image on the camera and CH <sub>4</sub> absorption profile at 4286ppm. ....	40
Figure 44 : CH <sub>4</sub> concentration monitoring at 1165ppm and 40000ppm. ....	40
Figure 45 : Performance of the single grating-based spectrometer.....	41
Figure 46 : Absorption profile at CH <sub>4</sub> 50ppm with 10cm-long gas cell. ....	41
Figure 47 : Zemax simulation to evaluate the spectral resolution of the single grating-based spectrometer.....	42
Figure 48 : Measured spectral resolution of the single grating-based spectrometer.....	42
Figure 49 : (left, top) Operation principle of the supercontinuum. (left, bottom) Working principle of the detection scheme. (right) Measured supercontinuum spectrum. ....	43
Figure 50 : Absorption measurement through a 10 cm long cell with (left) 40'000ppm CH <sub>4</sub> and (right) 1'165ppm CH <sub>4</sub> . The bottom part shows 5 single acquisitions, and the top part the corresponding HITRAN simulation.....	43
Figure 51 : Specification table for the NLIR 3055 up-conversion spectrometer, and schematic working principle.....	44
Figure 52 : Zemax model (left) and expected resolution / spectral range on the camera detector (right) for the final design.....	45
Figure 53 : Evolution of the multipass cell design. (left) second design and (right) third design. This required drastic adaptation to the spectrometer interface design. ....	46
Figure 54 : CAD of the single-grating based spectrometer prototype setup. ....	47
Figure 55 : (left) Example of a Zemax export. The definition of the optics is not readily compatible with mechanical CAD. (right) Location of the flip-mirror based by-pass system. ....	47
Figure 56 : Design of the FLAIR full prototype with overall dimension 45 x 35 x 35 cm <sup>3</sup> . ....	48
Figure 57 : (left) NIT camera acquisition and (right) corresponding column averaged spectrum. The red line illustrates the non-uniform gain pattern. ....	48

Figure 58 : Laboratory breadboard setup used during the optimisation phase.....	49
Figure 59 : Camera image for a halogen lamp.....	49
Figure 60 : CH4 50ppm monitoring results, using a lock-in amplifier.....	50
Figure 61 : Demodulated signal, using echelle grating-based 2D spectroscopy .....	51
Figure 62 : Simplified structure of gas sensing software algorithm .....	51
Figure 63 : List of all the equipment requiring electrical power. The power is provided either through battery packs, or the flying platform. ....	52
Figure 64 : NIT conference boot advertising the TACHYON 16k Camera and the FLAIR project. ....	55

## List of Acronyms

**Table 1: List of acronyms.**

Acronym	Meaning
CAD	Computer-Aided Design
COSMO	“Consortium for Small-scale Modeling” is a non-hydrostatic limited-area atmospheric modelling tool
CPU	Central Processing Unit
CTDAS	CarbonTracker Data Assimilation System
FLAIR	FLying ultraA-broadband single-shot InfraRed Sensor
GCS	Ground Control Station
IR	infrared
KET	Key Enabling Technologies
NUC	Non-Uniformity Correction
MIR	mid-infrared
MPC	multipass cell
NOAA	National Oceanic and Atmospheric Administration
ppbv	Part per billion in volume
OBC	onboard computer
OPOs	optical parametric oscillators
QCLs	quantum cascade lasers
RIA	Research and Innovation Action
SC	Supercontinuum
SNR	Signal-to-noise ratio
TCP	Transmission Control Protocol
UAV	Unmanned Aerial Vehicle



## 1 Introduction

**FLAIR - FLYing ultraA-broadband single-shot InfraRed Sensor** (H2020) is a Research and Innovation Action (RIA) funded by the European Union's H2020 programme under the Photonics Key Enabling Technologies (KET) topic.

The project seeks to address known challenges in the context of the significant effort that is observed nowadays in active air quality improvement. In order to be successful, these measures need be complemented by air quality monitoring at large scale to ensure compliance with air quality legislation but also to provide information for political decision making regarding air quality and safety. Large spatial coverage is particularly problematic outside the dense urban network of air quality monitoring stations. **FLAIR** proposes to close this gap.

The overarching objective of the project is the development of a compact, cost effective and high-performance air sampling sensor based on cutting-edge photonic technology, capable of performing high-specificity and high-sensitivity (ppbv) sensing over large areas as a result of its installation aboard an Unmanned Aerial Vehicle (UAV), commonly known as a drone.

Operating in the two atmospheric windows of 2-5  $\mu\text{m}$  and 8-12 $\mu\text{m}$  wavelength, the **FLAIR** sensor aims at detecting minute traces of molecules in complex gas mixtures from their characteristic infrared (IR) absorption fingerprints and provide real time information to the operator of the drone. The whole **FLAIR** system can operate in remote and/or dangerous areas and outside of established monitoring networks.

Directly targeted applications include air quality monitoring around industrial infrastructures, maritime and land based traffic, landfills and agriculture facilities. The sensor can also be used to coordinate emergency service response in the case of catastrophic events like wildfires, volcanic eruptions or chemical accidents.

Making the sensor airborne through its integration aboard a flying platform ~~a UAV~~ brings a clear advantage regarding system deployment and pervasive sensing over large areas. Additionally, due to the local character of its sensing operation, the **FLAIR** sensor can also provide data from inside optically dense clouds and plumes, which are usually not accessible by ground-based laser remote sensing methods.

Photonics technology is a promising approach to the challenge of air quality monitoring, as it can provide, in principle, accurate identification and concentration measurements of specific species in complex environments. Current solutions include several methods for air quality monitoring, among which are mass spectrometry, electronic noses and optical detection. While systems based on mass spectrometry are highly sensitive, they suffer from complexity and high footprint, which hinder integration on a flying platform ~~drone~~. Electronic noses are cheap but suffer from low accuracy.

Several systems based on light sources operating in the IR range, such as quantum cascade lasers (QCLs), diode lasers, optical parametric oscillators (OPOs) or frequency combs have enabled highly sensitive and selective detection of molecules. Such high performance tools, however, typically remain confined to academic research laboratories due to their narrow spectral operating window (covering only very few molecules), their operational complexity and their prohibitively high cost. These are the technical challenges **FLAIR** is addressing.

The **FLAIR** sensor will generate trace gas absorption spectra from which information on the levels of pollutants can be derived through adequate data processing.



This deliverable is linked to technical WPs 3, 4 and 5 covering the period from November 2017 to October 2018 (second year of the project).

## 2 Approach

This report was established by the participants listed in the table above, as foreseen in the project description, and under the lead of CSEM. More specifically, the following steps were taken:

- establishment of a first structure and draft (05.11.2019)
- contribution from partners (mid November 2019)
- second draft (02.12.2019)
- final report (05.12.2019).

## 3 Project progress overview

There was a change of coordinator from TEKEVER to RU in the spring of 2019. After that contract amendment, we went back on track. The interim payment helped DTU to start again and with the Guarantee fund, we have all partners again in financial balance. DTU managed to generate substantial light at long wavelength, from the new super continuum source and this source will be tested at RU on spectroscopy. The extension of the project helped to get this light source to be tested.

Concerning the mid infrared-based sensor, a detailed work plan is made towards the flight test in May 2020, with a helicopter. A company is identified, that flies for the Danish government. That company is sampling with a helicopter the exhaust of chimneys of large sea vessels in the waters around Denmark. We will place our sensor on board and test it in flying conditions above the ships. We will have in May several weeks to sample 120 vessels, so we can thoroughly test our sensor.

The sensor is now being finalized at CSEM and will be delivered to RU in the beginning of February 2020 where it will be tested. Then it will go for a measuring campaign to EMPA on a small zeppelin in Switzerland. As it is now, everything is on track.

## 4 Laboratory spectroscopy (WP3) results

Work package 3, led by RUN, includes the selection of relevant gas species, the definition of relevant system input parameters, development of a spectroscopic data processing software for real-time monitoring.

<b>Lead partner</b>	RUN
<b>Contributing partners</b>	SA, NKT, NIT, CSEM

During this period the finalized NIT Tachyon16K MIR camera has been tested for spectroscopy application.

### 4.1 Detection of a 1D dispersed beam on the camera

We used a MIR super continuum and a single diffraction grating to disperse the beam on the camera. The super continuum beam is sent through the multipass cell (filled with atmospheric air) to maintain the attenuation of the power the same as the real operational system. We detect a stripe on the camera as shown in Figure 1.

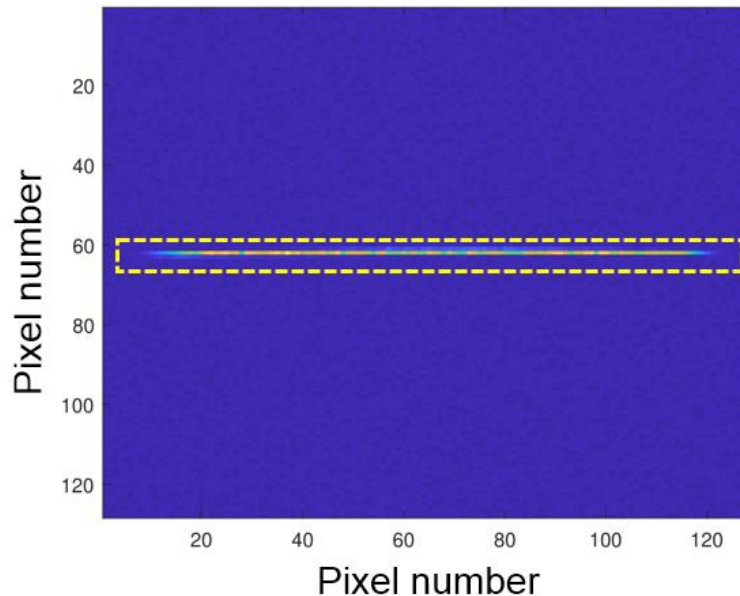


**Figure 1 : The stripe form the diffracted broadband light on the camera**

We record the data using the binary output file option. Since the width of the stripe on the camera occupies three rows of pixels, we integrate values of the readouts from the camera for three vertical rows (row #58-#60 where the spectrum lies indicated by the yellow box in Figure 1) to achieve the spectrum. The result is shown in Figure 2(a) for 10 consecutive camera shots (in different colours). Note that we have subtracted the DC background in the readout to have the baseline around zero. The camera parameters are Bias = 2.00 V, Tint = 100  $\mu$ s, Frame rate = 500 Hz, and Black level = 4000. To obtain the dark noise of the camera we do the same analysis for three consecutive rows of the camera with no illumination, namely vertical rows #79-#81. The result is shown in Figure 2(b) for 10 consecutive camera shots (in different colours). The standard deviation of the noise where no light intensity is on the camera is around 5.8 units. Note that the digitization noise can also be seen on the detector output in a single shot (see Figure 2(b)). Also note that the persistent fluctuations of the intensity on the illuminated pixels cannot be due to the spectral envelope of the super continuum source, since this envelope is varying slowly in terms of the wavelength. We saved 10000 shots of the camera and averaged each 1000 shots to achieve 10 consecutive averaged measurements. The results of these 10 consecutive averaged measurements are shown in Figure 3(a) and (b) where the same camera rows are integration as discussed for Figure 2. The sharp structures stay on the recorded spectrum, even after averaging. The standard deviation of the noise where no light intensity is on the camera is around 4.1 units. This shows that the camera dark noise is not white (since the noise level is not decreased by the square root of the number of averaged shots) and more importantly averaging would not help to reduce the noise level. Moreover a zoom into the noise at some specific set of pixels, shows a strong correlation among these 10 averaged measurements. Figure 3(c) for instance shows an enlargement around pixels #112 to #121, where the correlation is very strong.

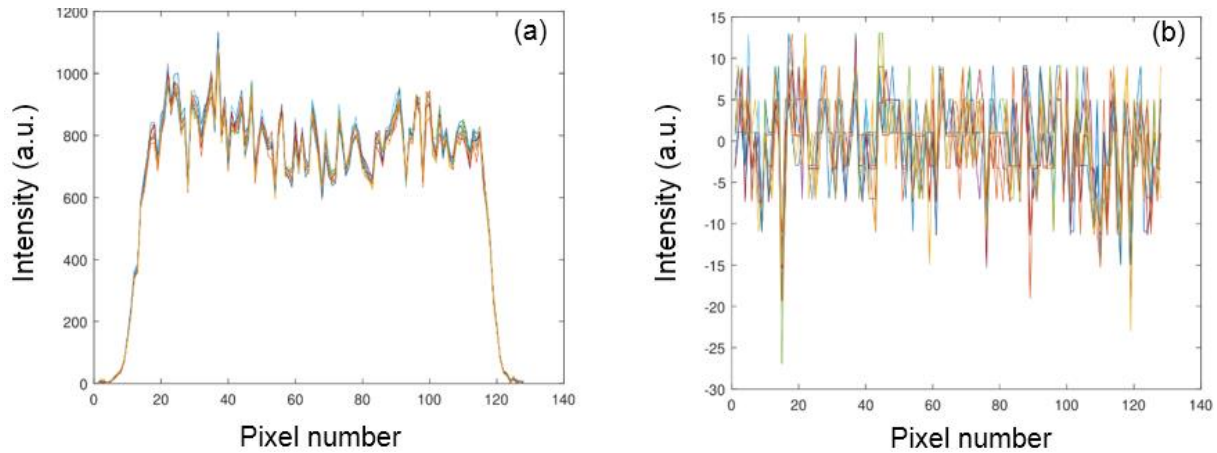


**Figure 2 : (a) The recorded spectra for 10 consecutive camera measurements. (b) The recorded dark noise for 10 consecutive camera measurements. The details of the measurements are explained in the text.**

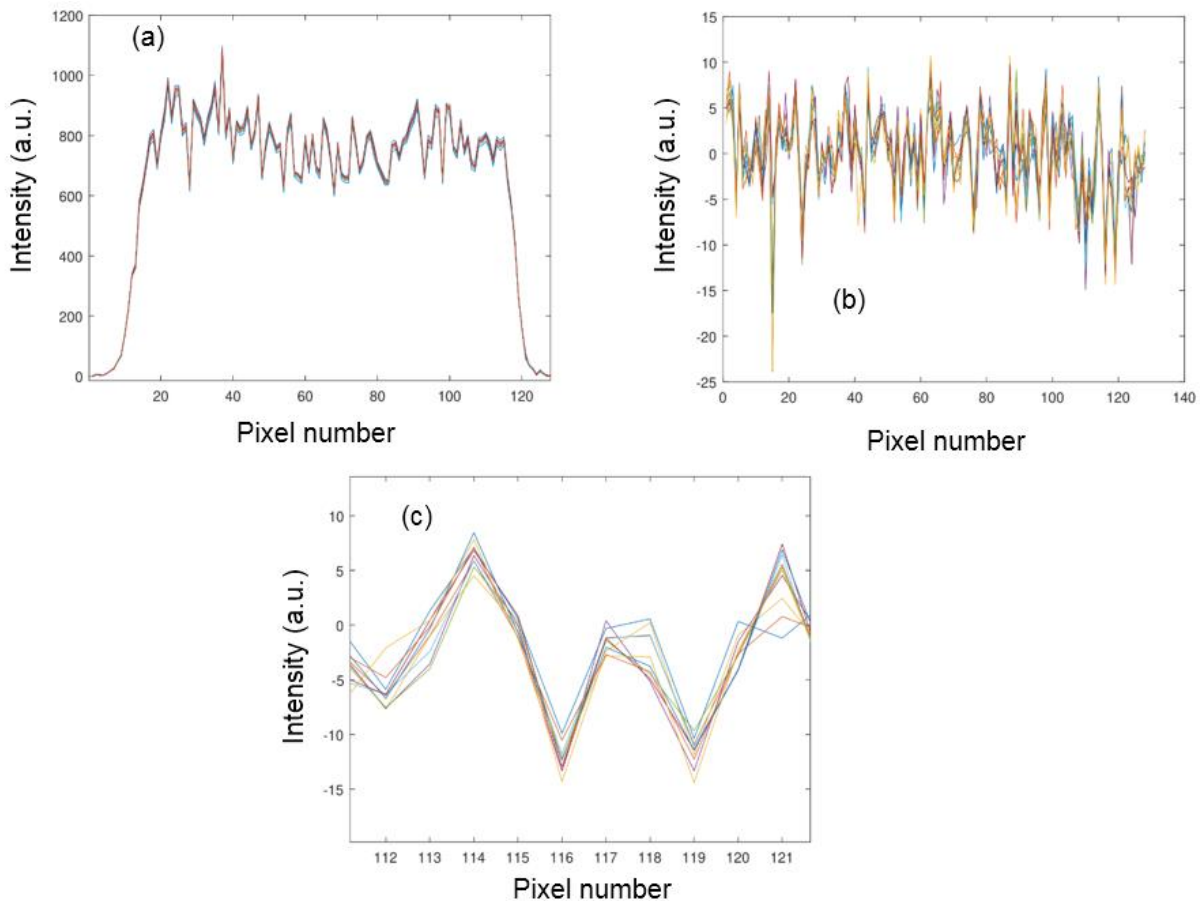


**Figure 3 : (a) The recorded spectra for 10 consecutive, 1000 averages camera measurements. (b) The recorded dark noise for 10 consecutive, 1000 averages camera measurements. The details of the measurements are explained in the text. (c) A zoom around pixels #11**

As it is mentioned in the Annex 2 of the NIT Visualization software manual:

*"It is well known that the performance of FPAs (focal-plane arrays) is known to be strongly affected by the spatial non-uniformity in the photoresponse of the detectors in the array, also known as fixed-pattern noise, which becomes particularly severe in mid- to far-IR imaging systems. Individual elements in the FPA differ in responsivity to incoming irradiance, which is the main reason why fixed pattern noise*

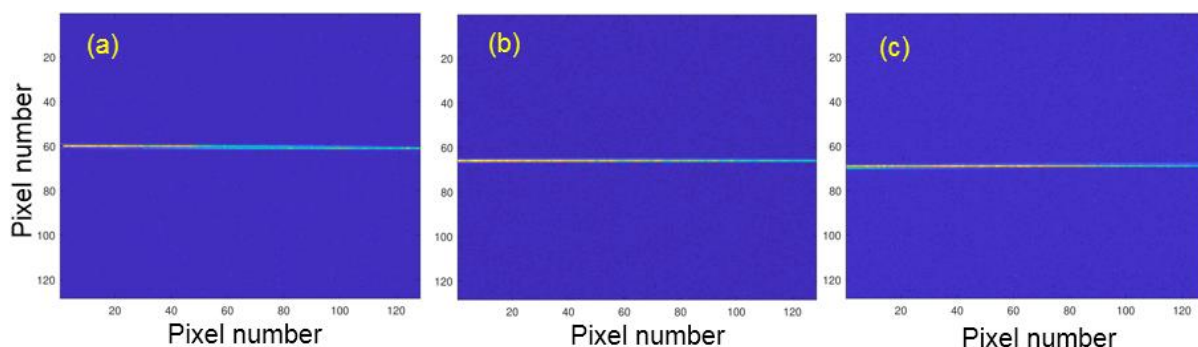
occur in an image. Some pixels end up too bright, some too dark, depending on a multitude of parameters. Some of these parameters may be identified in advance and compensated for, but it is impossible to compensate for all. The result is an image with a superimposed pattern that varies with unknown environmental parameters, leading to a time varying fixed pattern noise. Despite the advances in detector technology in recent years, detector non-uniformity continues to be a serious challenge, degrading spatial resolution, radiometric accuracy, and temperature resolvability. Moreover, what makes the non-uniformity problem more challenging is the fact that spatial non-uniformity drifts slowly in time; thus a one-time factory calibration will not provide a permanent remedy to the problem.

No uniformity correction (NUC) techniques are categorized into two classes, namely, calibration-based and scene-based techniques. In the commonly used two-point calibration technique for example, the normal operation of the FPA is halted as the camera images a uniform calibration target (typically, a blackbody radiation source) at two distinct and known temperatures. The gain and the bias of each detector are then calibrated across the array so that all detectors produce a radiometrically accurate and uniform readout at the two reference temperatures. Scene-based correction algorithms, on the other hand, do provide significant cosmetic NUC without the need to halt the camera's normal operation; however, this convenience comes at the expense of compromising radiometric accuracy. Scene-based techniques typically use an image sequence and rely on motion (or changes in the actual scene) to provide diversity in the scene temperature per detector. This temperature diversity, in turn, provides a statistical reference point, common to all detectors, according to which the individual detector's responses can be normalized."

Therefore, with no non-uniformity correction, each pixel of the camera has a different photo response (gain) and offset (dark current), whose values tend to drift slowly in time as well. Since we do not have a blackbody radiation source in our lab and also the impossibility of using a blackbody radiation source in the final flying sensor for a regular calibration – due to the limitation of weight, volume and power consumption – we characterize the operation of the camera for spectroscopy without any non-uniformity correction.

## 4.2 Recording the same 1D spectrum on different pixel arrays

In the second test we use the same setup as the first test, but this time measure the stripe on the detector at three different horizontal pixel arrays on the detector, by slightly steering the beam to the camera on the vertical direction. Figure 4(a) to (c) shows the camera image from the dispersed stripe at the three different beam heights averaged for 1000 times. The corresponding spectrum is shown in Figure 4(d) to (f). In ideal camera operation these three spectra should be very identical (only differ in noise).



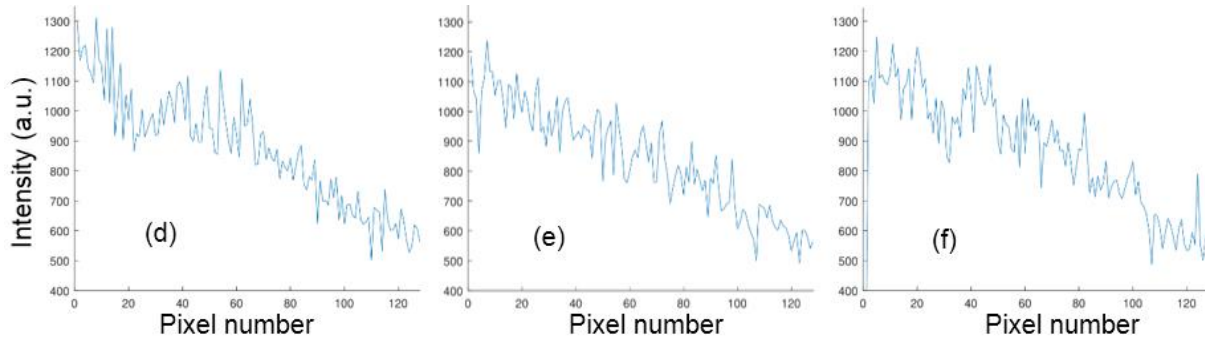


**Figure 4 : (a) to (c) The stripe from the diffracted broadband light on the camera measured at three different beam high with three different rows of pixels. (d) to (f) the corresponding measured spectra from (a) to (b) images respectively.**

To compare these responses we plot them on a single plot shown in Figure 5. The different photo responses of different pixels are quite obvious, which make a noise-like response on the spectrum known as the fixed-pattern noise. The maximum intensity of the spectra is ~1200 and the standard deviation of the fixed-pattern noise is ~100, thus the effective SNR of the spectrum is ~12. This value is roughly the same for a single shot measurement as well and averaging will not improve it. This issue drastically limits the sensitivity of any 2D spectrometer based on the camera.

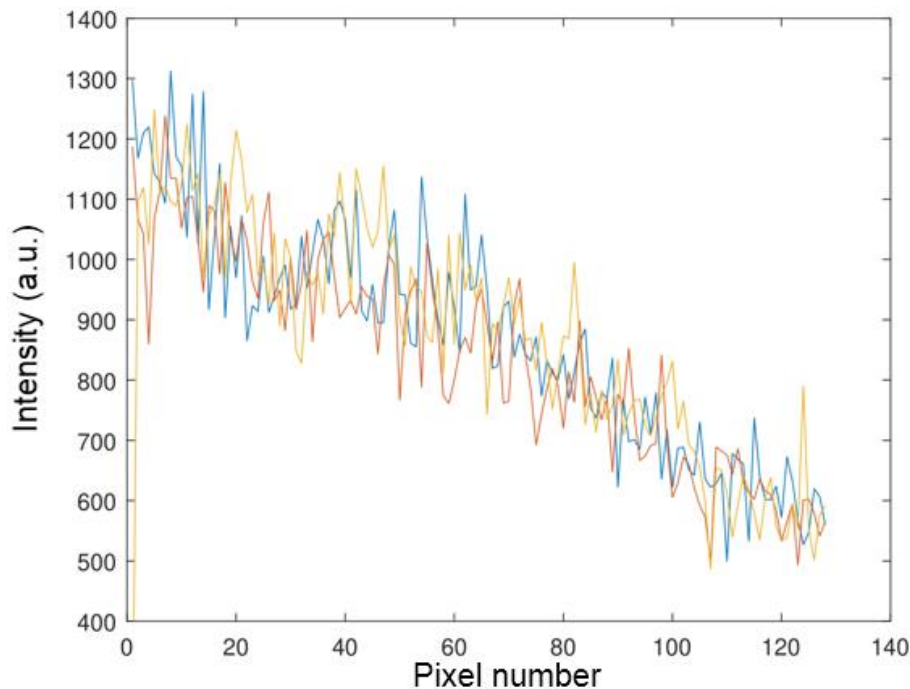


**Figure 5 : The same 1D spectrum measured with three different rows of the camera.**

### **4.3 Recording the same 1D spectrum with different bias voltages**

We also measured the detected stripe with the same row of the pixels in the camera (1000 averages), but with three different camera bias voltages. Figure 6(a) shows a record of the stripe for three different bias voltages (1.50 V, 1.75 V, and 2.00 V) and (b) shows the normalized spectra. Although the measured spectra looks similar in panel (a), the normalization reveals some discrepancy in panel (b). Therefore different bias values can also change the response of the pixels, however; this effect is much less severe than the nonuniformity of the photoresponse of different pixels.



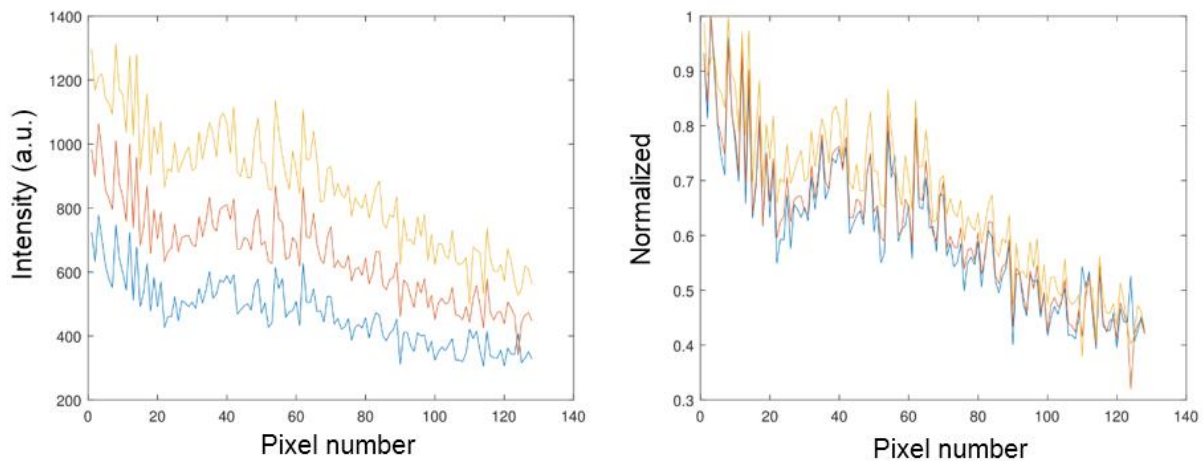


Figure 6 : (a) The same 1D spectrum measured with three different camera bias voltages (blue curve 1.50 V, red curve 1.75 V, and yellow curve 2.00 V). (b) The normalized spectra measured in (a).

#### 4.4 Recording the same 1D spectrum with different integration times

To test the effect of the integration time, we measure a 1D spectrum with the same row of pixels and the same bias voltage (1000 averages), but with two different integration times. Figure 7 shows the results. The normalized spectra in panel (b) show a very good agreement, suggesting that different integration times would not affect the response of the camera.

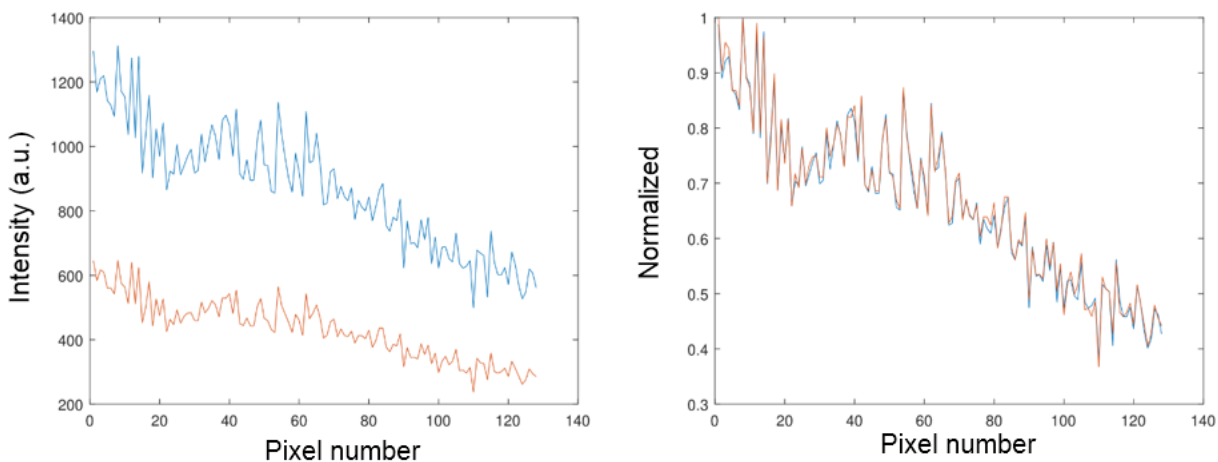


Figure 7 : The same 1D spectrum measured with two different camera integration times (blue curve 200  $\mu$ s and red 100  $\mu$ s). (b) The normalized spectra measured in (a).

#### 4.5 2D spectrum of CH<sub>4</sub>

To verify these observations in a spectroscopy setup, we developed a simple 2D spectrometer using an Echelle grating and a prism instead of the ruled grating. We also put a 30 cm gas cell filled with 100% CH<sub>4</sub> in the path of the beam. Figure 8 shows the measured background and signal image spectra in panel (a) and (b) respectively. Note that no attempt was made to optimize the alignment of the 2D spectrometer (e.g. to fill the area of the camera as much as possible), since we are only validating the sensitivity of the camera. We compensate the skew of the image on the camera as is shown in Figure 8(c) and (d) in the post-processing, and retrieve the absorption spectrum. A single shot measurement of the signal (in red) and background (in blue) is shown in Figure 9 panel (a) and the subtraction of the signal and

background is shown in panel (b). At an intensity of  $\sim 600$ , the standard deviation of the noise is  $\sim 50$  units. This yields an SNR of  $\sim 12$ .

And finally to verify that averaging would not improve the signal to noise ratio, we average output of the camera for 1000 shots and perform the same presented signal processing. The signal (in red) and background (in blue) is shown in Figure 10 panel (a) and the subtraction of the signal and background is shown in panel (b). No SNR improvement is achieved after averaging.

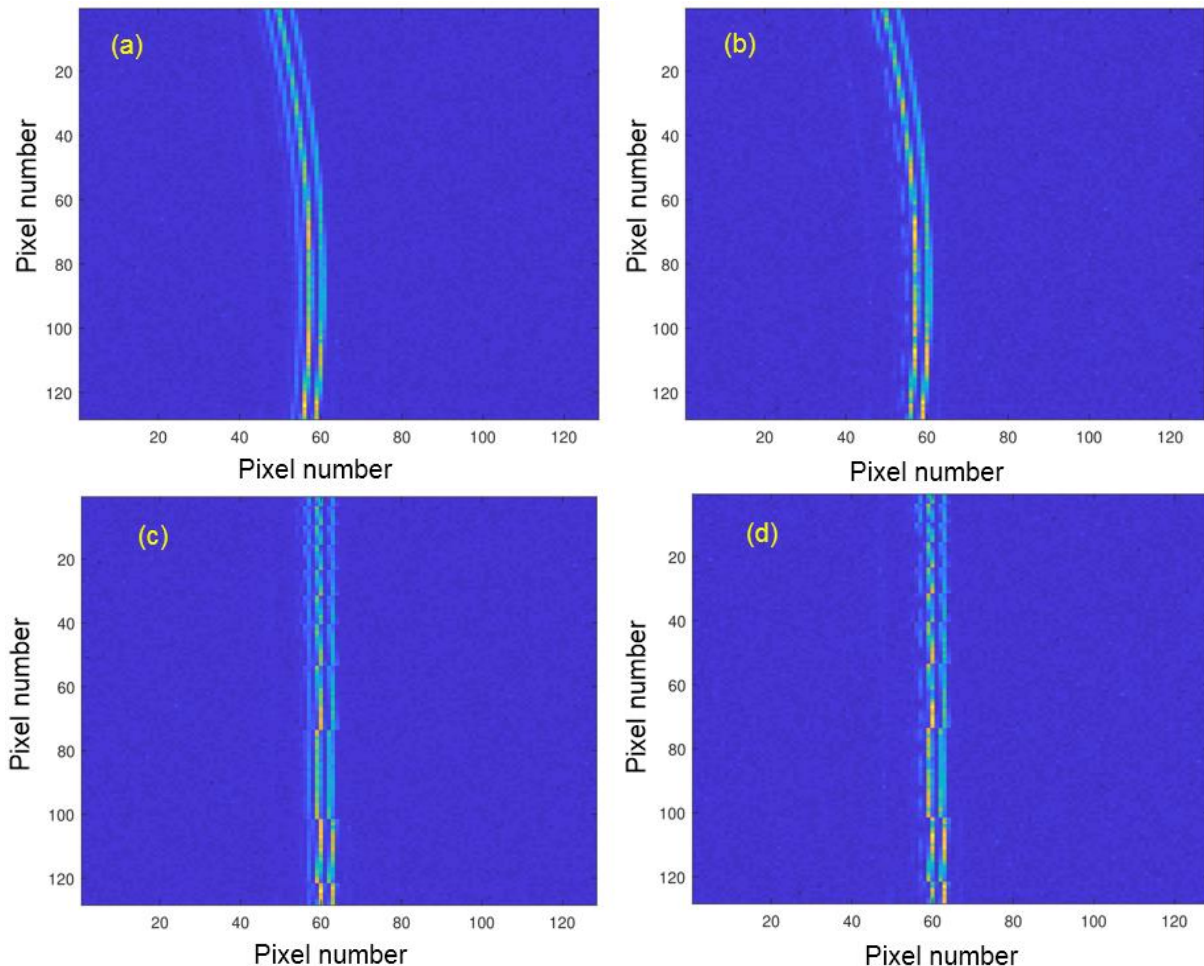


**Figure 8 : Measured (a) background (lab air sample) and (b) signal (100% CH4 sample) image spectra, as well as the same corresponding spectra for background and signal after removing the image skew in (c) and (d) respectively.**

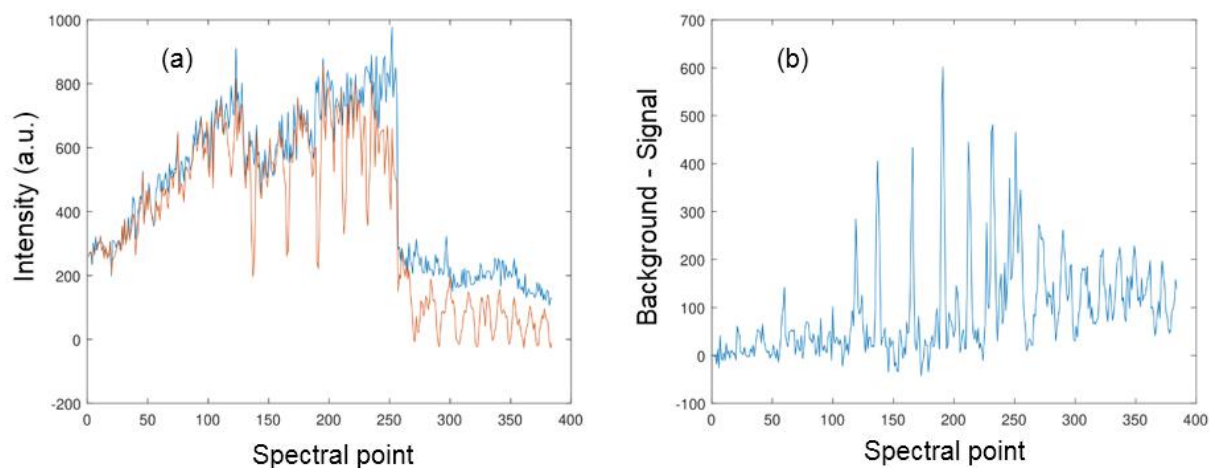




**Figure 9 : (a) single shot measurement of the signal (in red) and background (in blue). (b) the subtraction of the signal and background.**

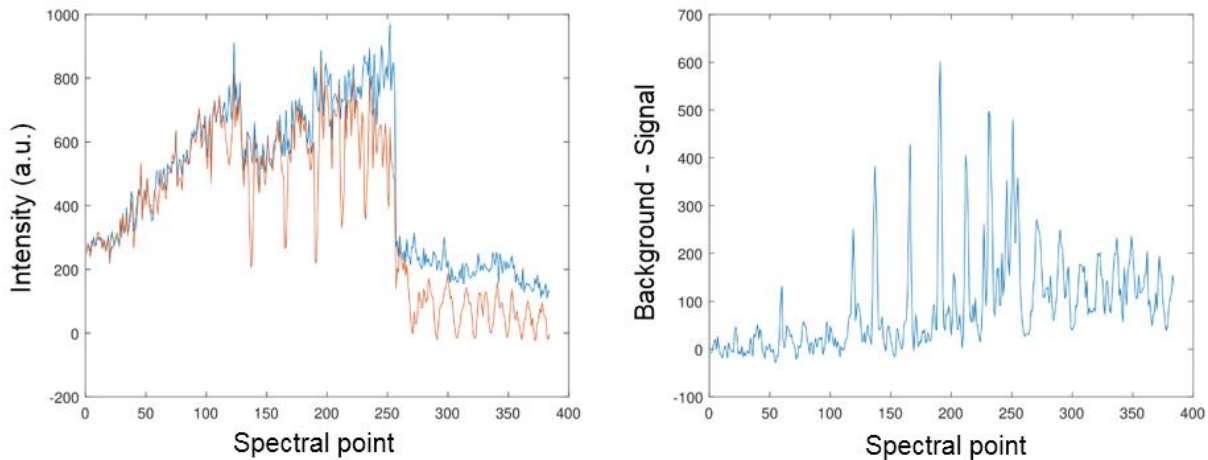


**Figure 10 : (a) 1000 average measurement of the signal (in red) and background (in blue). (b) the subtraction of the signal and background.**

#### **4.6 1D dispersed beam on the camera before and after NUC**

Same as before, we used a MIR super continuum and a single diffraction grating to disperse the beam on the camera. The super continuum beam is sent through the multipass cell (filled with atmospheric air) to maintain the attenuation of the power the same as the real operational system. We detect a stripe on the camera as shown in Figure 11.

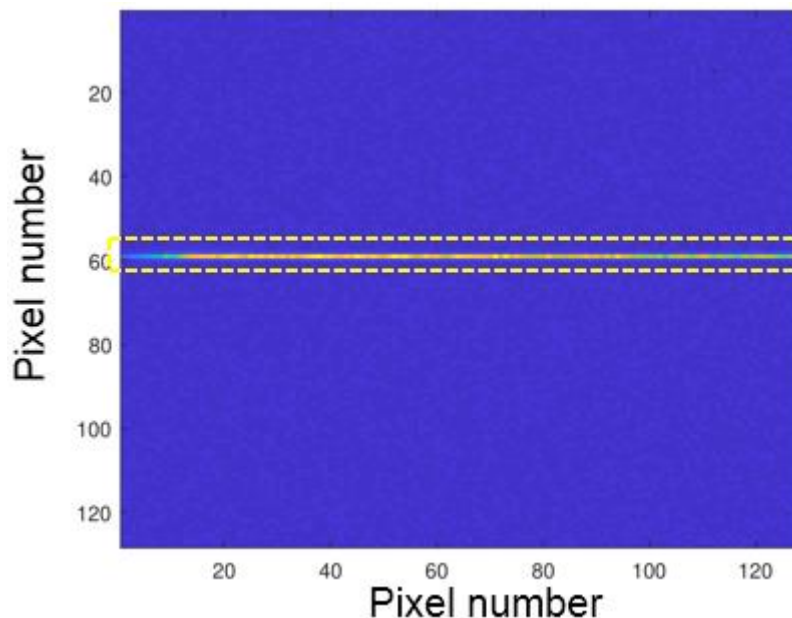


**Figure 11 : The stripe from the diffracted broadband light on the camera.**

We record the data using the video format (.dat file format), saving an image each 100 ms. Since the width of the stripe on the camera occupies around 3 rows of pixels, we integrate values of the readouts from the camera for three adjacent rows (row #59-#61 where the spectrum lies indicated by the yellow box in Figure 11) to achieve the spectrum. The result is shown in Figure 12(a) for 20 camera shots (in different colors). Note that we have subtracted the DC background in the readout to have the baseline around zero. The camera parameters are Bias = 2.00 V, Tint = 200  $\mu$ s, Frame rate = 500 Hz, and Black level = 4000. To obtain the

dark noise of the camera we do the same analysis for three consecutive rows of the camera with no illumination, saved after closing the camera shutter for the same consecutive rows (#59-#61). The result is shown in Figure 12(b) for 20 camera shots (in different colours). The average spectrum and dark noise of these 20 camera images are shown in Figure 12(c) and (d), respectively. The standard deviation of the noise where no light intensity is on the camera is around 9.5 units for a single measurement and 7.0 for 20 averages. The persistent fluctuations of the intensity on the illuminated pixels are due to the fixed-pattern noise of the camera. The fixed-pattern noise is around 120 units that limits the SNR to  $\sim 13$ , which is in consistence with the results from the previous report.

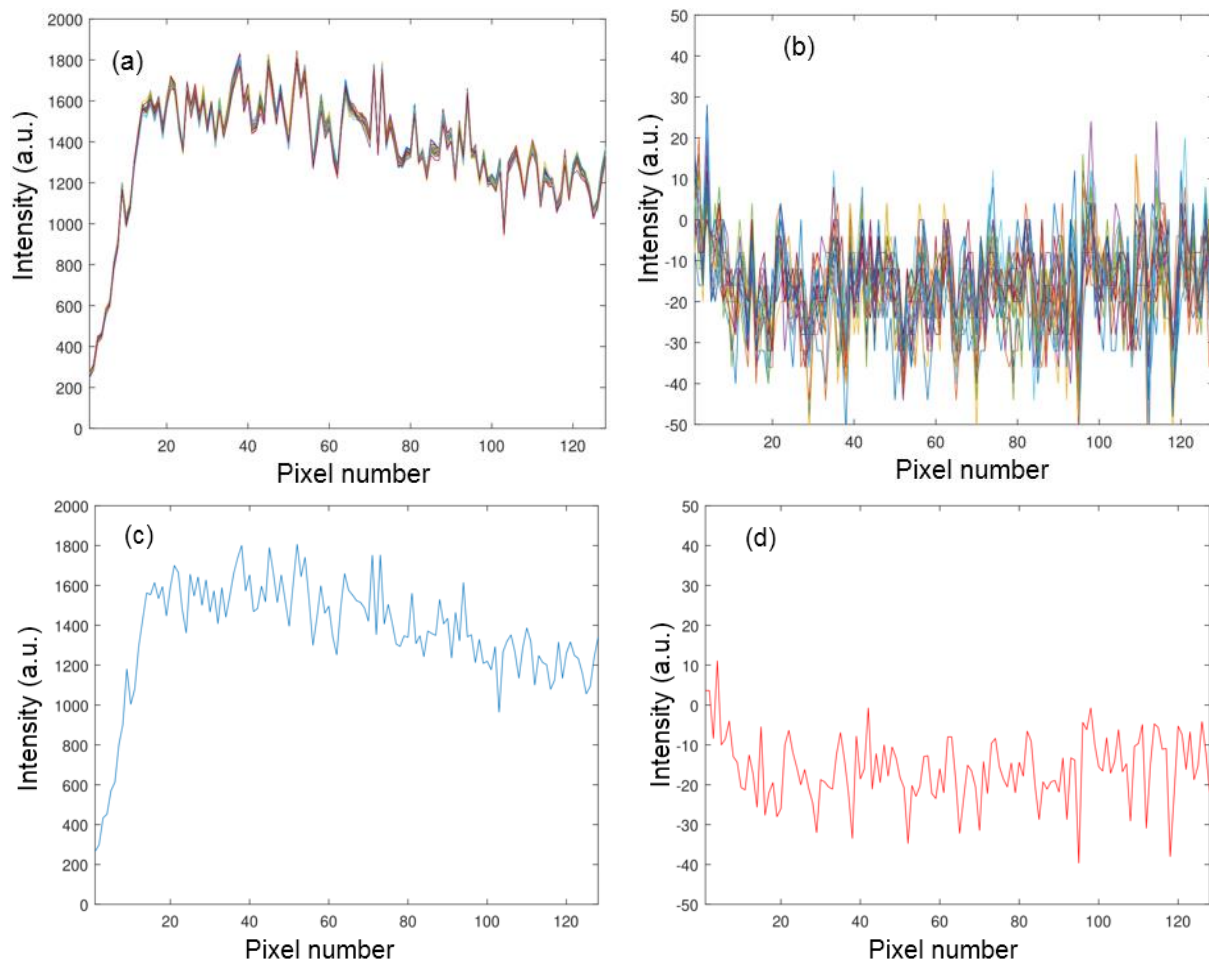


**Figure 12 : (a) The recorded spectra for 20 camera measurements. (b) The recorded dark noise for 20 camera measurements. (c) The averaged spectrum and (d) the averaged dark noise. The details of the measurements are explained in the text.**

The same measurement is shown in Figure 13, but this time after nonuniformity correction (NUC) of the camera. The NUC measurement was performed in NIT a few days after the spectrum was measured in Radboud University. It was consisted of applying the NUC for the camera gain (each pixel) and one point offset calculation (for more details on the NUC procedure contact NIT). The measured spectra and noise for 20 camera images as well as the average spectrum and dark noise of these 20 camera images are shown in Figure 13 (a) to (d). The standard deviation of the noise where no light intensity is on the camera is around 6.6 units for a single measurement and 2.0 for 20 averages. This shows a noise reduction factor of 3.3 for 20 averages, which is close to the reduction factor expected from white noise ( $\sim 4.5$ ), and is much better than the results without NUC. The fixed pattern noise is around 40 units that is around a factor of 3 better than the results without NUC and is limiting the SNR to  $\sim 40$ .

Note that although the dark noise behavior is drastically closer to white-noise regime, the SNR is still limited by the fixed pattern noise of the camera which cannot be improved by averaging.

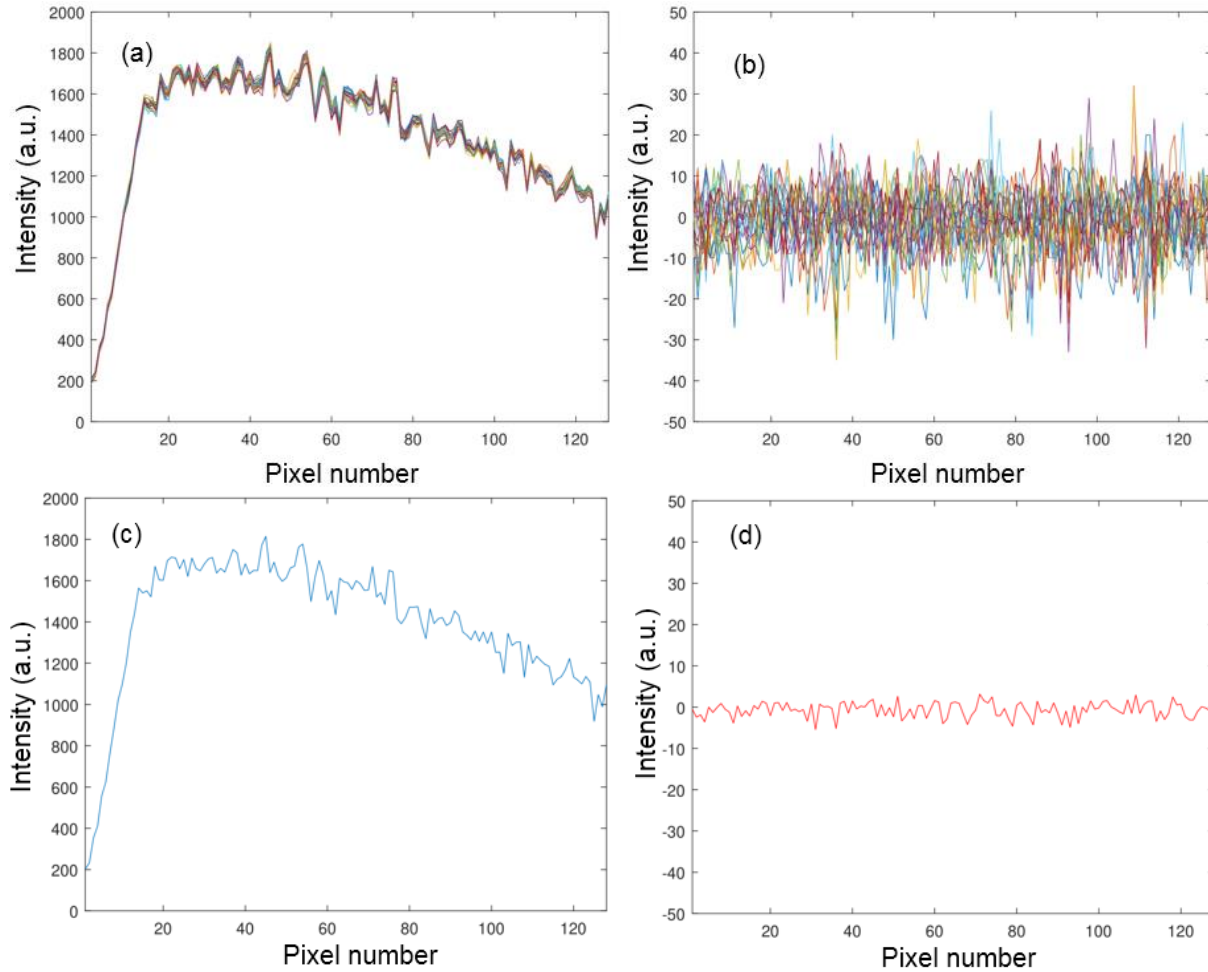


**Figure 13 :** (a) The recorded spectra for 20 consecutive measurements. (b) The recorded dark noise for 20 consecutive measurements. The details of the measurements are explained in the text. (c) The average spectrum and (d) the average dark noise.

#### **4.7 The same 1D spectrum on different pixel arrays before and after NUC**

In the second test we use the same setup as the first test, but this time measure the stripe on the detector at three different horizontal pixel arrays on the detector, by slightly steering the beam going to the camera on the vertical direction. Figure 14(a) to (c) shows the camera image from the dispersed stripe at the three different beam heights averaged for 20 times. The corresponding spectrum before NUC is shown in Figure 14(d) to (f), and after NUC in Figure 14(g) to (i). The reduction of the fixed-pattern noise is obvious after NUC, especially in panel (g) compared to (e). Note that after an ideal NUC operation the three spectra [panel (g) to (i)] should be very identical (only differ in noise).

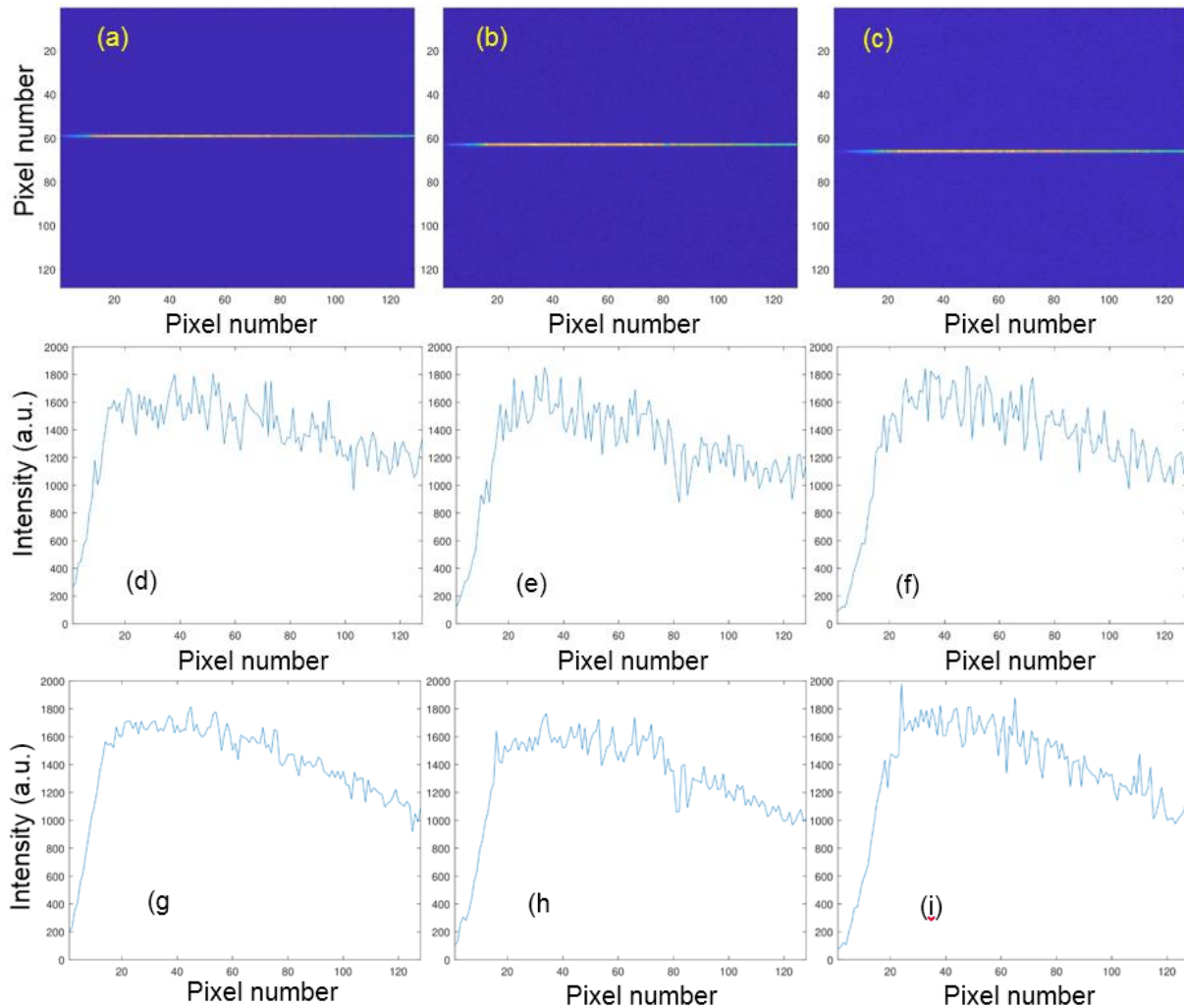


**Figure 14 : (a) to (c) The stripe from the diffracted broadband light on the camera measured at three different beam high with three different rows of pixels (averaged 20 times). (d) to (f) depicts the corresponding measured spectra from (a) to (c) images, respectively, before NUC and (g) to (i) shows the same spectra after NUC.**

To compare the spectra before and after NUC we plot the corresponding spectra on a single plot shown in Figure 15(a) and (b) in different colors. We shifted the spectra on x-axis to correct the slight drift in the measurements. The corresponding dark noise before and after NUC is also shown in panels (c) and (d). Although the dark noise is drastically reduced after NUC, but the SNR is not enhanced dramatically due to the remaining fixed-pattern noise. Also as mentioned earlier the SNR will be limited to  $\sim 40$  and cannot be improved by averaging or (most probably) modulation-demodulation techniques, since the fixed-pattern noise is time and frequency independent.

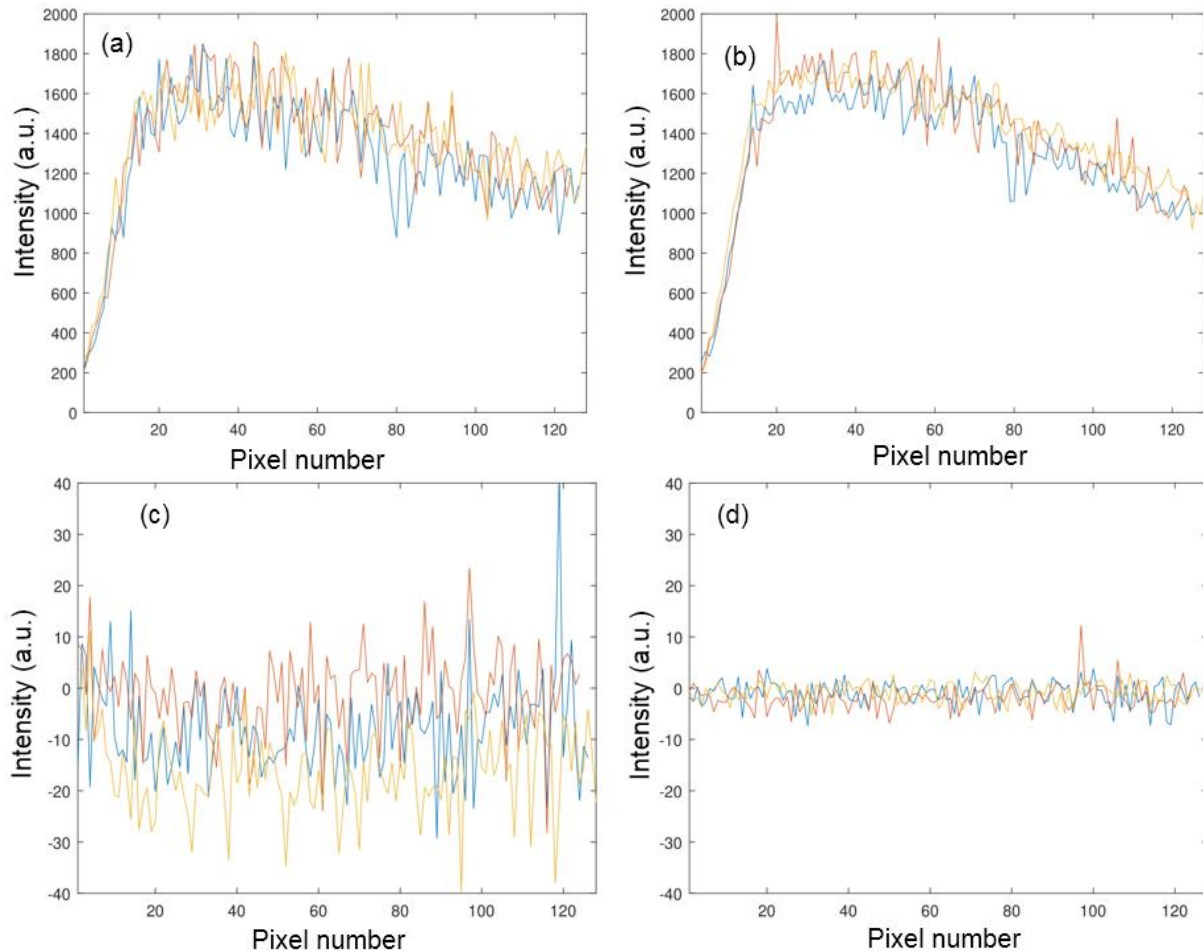


**Figure 15 :** The same 1D spectrum measured with three different rows of the camera as the previous figure (in different colors) in (a) before NUC and (b) after NUC. (c) and (d) depict the dark noise of each different row before and after NUC, respectively.

## 4.8 Conclusions

We can summarize the results of the applied verifications in five key points.

Without (dynamic) no uniformity correction (NUC):

1. Since the dark noise on each pixel is not white, each pixel has a different dark current (or offset voltage) and as a result averaging will not increase the SNR of the measurement.
2. Since the photo response of each pixel is different the recorded spectrum has ~8% fluctuations pixel by pixel or “fixed-pattern noise” which imposes that the SNR is always limited to ~12 in an actual measurement with no improvement from averaging.

With (dynamic) no uniformity correction (NUC):

3. NUC reduces the dark noise by a factor of ~2, and more importantly the dark noise after NUC can be also reduced by averaging (at least up to 20 images). The dark noise after NUC behaves close to white noise; the noise roughly decreases by the square root of the number of averages. Although this is a good improvement, but the final measurement is still limited by the fixed-pattern noise, not the dark noise.



4. NUC reduces the fixed-pattern noise by a factor of  $\sim 3$ ; however, averaging would not help to reduce the fixed-pattern noise even after NUC. Therefore the best achievable SNR will be  $\sim 40$  in an actual measurement (yielded from a single measurement) with no improvement from averaging.
5. We can use these results to estimate the sensitivity of the developed sensor for detecting CH<sub>4</sub>. With 10 m interaction length, 1 GHz spectral resolution, and SNR of 40;  $\sim 1$  ppm CH<sub>4</sub> detection limit can be expected in an acquisition time of 2 ms (500 FPS). Note that this sensitivity cannot be enhanced by averaging. Better NUC process can obviously enhance the SNR and as a result further improve the sensitivity of the sensor.

## 5 Sensor subsystems development (WP4) results

Work package 4, led by CSEM, includes the development of the **FLAIR** sensor itself, comprising the development of each subsystem and final integration and prototype testing.

<b>Lead partner</b>	CSEM
<b>Contributing partners</b>	RUN, SA, NKT, NIT, DTU, EMPA, CSEM

### 5.1 Supercontinuum sources

#### 5.1.1 2-5 $\mu$ m source

The super continuum source developed for the FLAIR project was redesigned. The details of this redesign are covered in detail in deliverable D4.1.2. The new super continuum light source developed in the FLAIR project is seeded by an amplified diode laser centred at 1.56  $\mu$ m that produces nanosecond pulses at a repetition rate of 200 kHz and an average power of 1 W. This is an improvement on the previous laser for a number of reasons. For one, the laser has a higher repetition rate (200 vs 30 kHz), meaning pulse energy is no longer a significant limiting factor in our laser system. This was a constant problem in our previous system, regularly causing failures between the silica-ZBLAN interface. The laser is also higher power (1 vs 0.6 W), meaning more power can be transferred to the wavelengths of interest. As we will discuss later, this improvement is a factor of 10. The laser is also more stable. Although we have no quantitative data for this, it is clear from qualitative observation that the laser has significantly lower short- and long-term fluctuations. This can also be attributed to improved packaging. The fiber lengths used in the new optimized source are similar to the ones used previously.

The packaging of the optimised supercontinuum source has been redesigned to fit into a larger 220x150x55 mm casing (see Figure 16). This is to allow more space for the fibre coil and more room for inbuilt heat sinking of the seed laser. The amplified laser diode is a BkTel prototype nanosecond source as described above, and requires control circuitry, and interfacing electronics. In the previous system, there was considerable issues with heat stability which resulted in power fluctuation and a limited possible integration time before the SNR became affected. To help solve this, the packaging was designed with more heat sinks, in particular sandwiching the laser between two heat sink plates. This also ensures the mechanical stability of the laser. Using this method, the temperature of the system can be kept between 30-35 °C, in contrast to the previous laser which would settle around 41 °C. The increased packaging size of the box also aids in the cooling, with more space available to circulate air.

The other part of the laser source we need to consider when packaging is the series of optical fibres including passive silica, rare-earth doped silica and ZBLAN. In the previous source,

stress and twist induced on the fibres in the tightly confined box affected loss and polarisation of the signal, as well as strength and lifetime of the splices. That is to say, after several days in the enclosure it was not uncommon for a splice to break without any additional perturbation. This was improved in the optimised source by using a larger enclosure so that bend radii were larger.

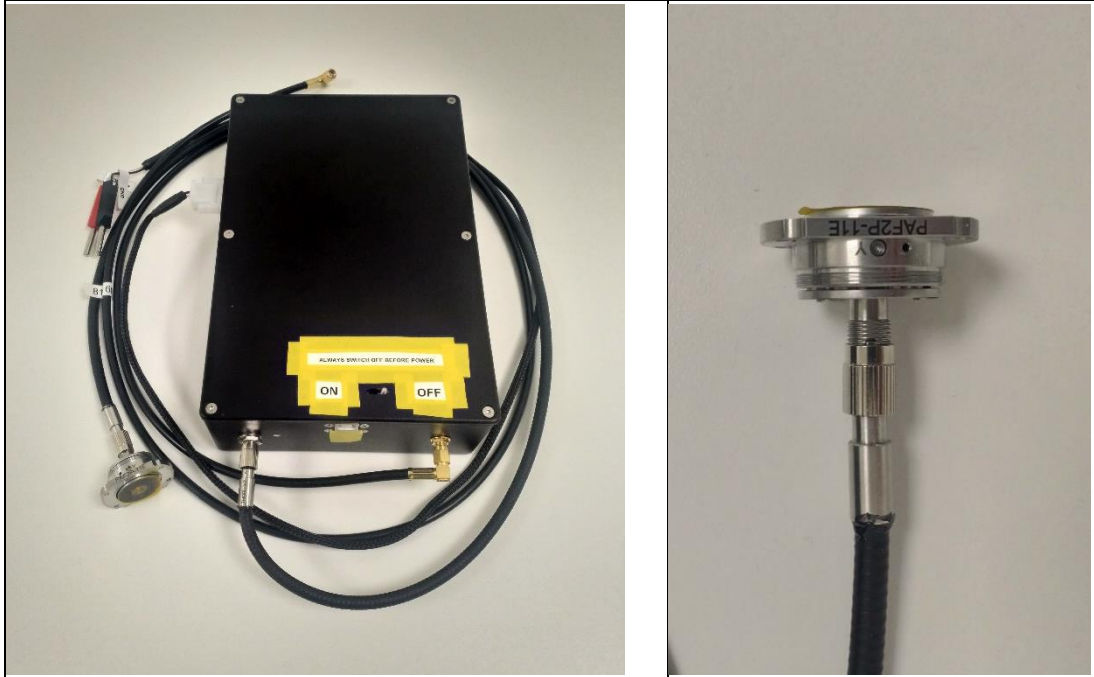


**Figure 16 : Packaging of the super continuum source showing compact 220x150x55 mm dimensions and output armoured cable with collimating Thorlabs fiber port on the output.**

Finally, the packaging is interfaced with a USB type B connector that allows monitoring of internal parameters (e.g. temp) and for adjustment of current settings. It is powered by a 24V DC supply that requires around 0.5A, and is triggered by a 0-2.5V (floor-ceiling), 200 kHz laser. If the current is set to the desired level in advance, the laser can be operated through an on-off switch on the top of the enclosure.

At the output port facet of the laser, the following optical characteristics in Table 2 were recorded using a long-pass filter (passes wavelength above the given value). These can be compared to Figure 18, which shows the spectrum of the laser in linear (top panel) and logarithmic (bottom panel) scale between 2-5  $\mu\text{m}$ .

**Table 2 : Long-pass filtered measurements of the laser's output power.**

Cutoff wavelength	Optimised laser system output power (mW)	Previous laser systems output power
Total	150	15
2500	60	5.0
3000	44	4.1
3500	11	1.8

The temporal optical power stability of the optimized supercontinuum was measured at CSEM with a S302C detector from Thorlabs over 16 hours during the night, as shown in Figure 17. When the laser was switched on, the laser output power tended to gradually increase in time from 142mW to 158mW. The power stabilized after approximately 3 hours after turning on the laser. This could be attributed to thermal effects and could be affected by temperature variations in the room. This will be investigated further at a later date.



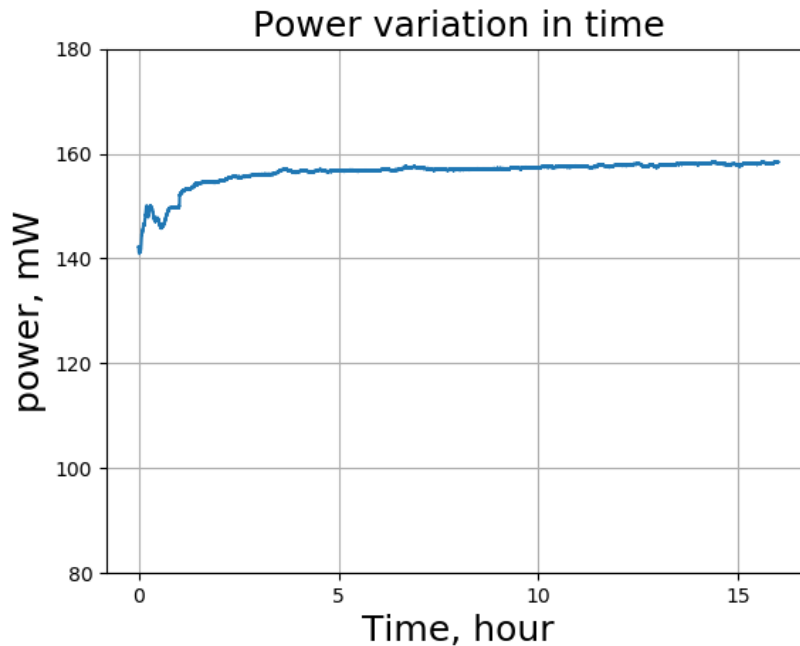


**Figure 17 : Power variation of the supercontinuum source measured over a 16h period.**

One can make a number of observations from this new data. First, we can see the total power difference between the new and old system is a factor of 10, which holds approximately true for higher cut-off wavelengths. By also considering the repetition rate difference, we can infer a difference in pulse energy of 1.5x (the new system has more energy).

We can also see from Figure 3 that significant power is held above 3  $\mu\text{m}$ , with a strong peak at 3.4  $\mu\text{m}$ . This will be useful for the intended purpose, where spectroscopic measurements will focus on molecules at 3.3  $\mu\text{m}$ . In contrast to the previous spectrum (shown in Figure 19), we can see both that the peak is better located, and there is also more available signal between 2-3  $\mu\text{m}$ .

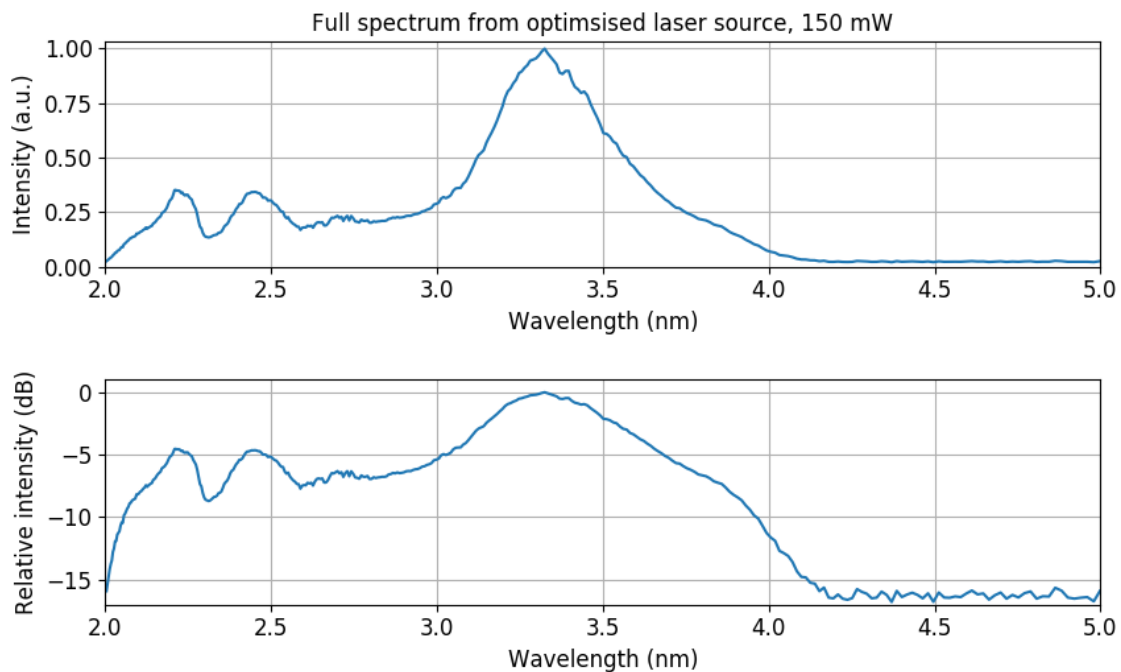


**Figure 18 : Output spectrum of the optimised laser system.**

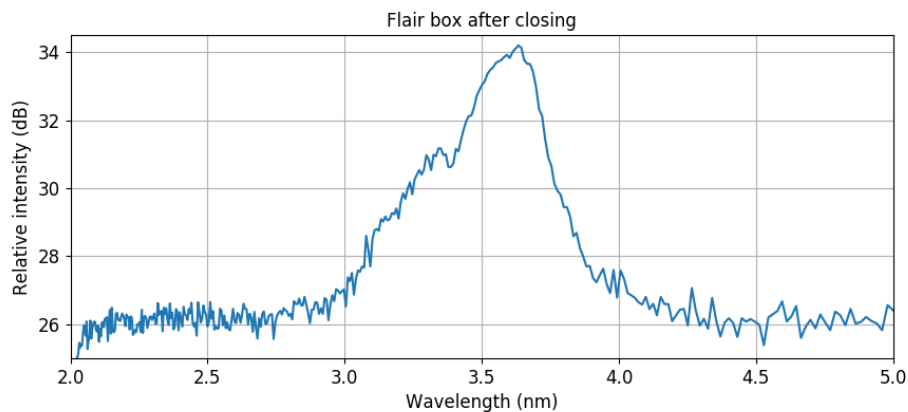


**Figure 19 : Output spectrum of the previous laser system.**

Some months at the end of development of this deliverable were devoted to developing an interfacing apparatus to take the uncollimated light from the fibre end and inject it into the multi-pass cell. To design this, we need to take the divergent light and focus it through a lens at such a detuning that a  $2^\circ$  angle is created with a tunability of  $\pm 1^\circ$ . This will ensure beam waist alignment with the input and output of the multi-pass cell is possible and result in high throughput.

To achieve a robust design, a Thorlabs fiber port with a black diamond 11mm focal length lens is used (shown in Fig 5). This is intended for collimation but can be adapted by offsetting the spot distance from the lens by 1-2 mm, thus moving the focal point of the apparatus to around 120 mm; a distance consistent with a  $2^\circ$  divergence. The offset was achieved by milling a stainless-steel fibre ferrule from 10 mm down to 1mm and inserting the small spacer into the barrel of the fiber port. This leaves a free-space channel for the beam but will prevent complete tightening of the connector around the fiber port thread.

We have experimentally demonstrated this change in focal point, implying the divergence angle is correct. Due to the design of the fiber port, the apparatus is also tunable in the x-y by 1.4 mm, and in the z-direction by  $\pm 1$  mm, corresponding to an angular tunability of  $0.7$ - $2.8^\circ$ . The z-direction tunability also induces beam steering, which can be used to gain further improvements in multi-pass cell throughput.



**Figure 20 : Focusing fiber port (left) and stainless-steel ferrules (right).**

### 5.1.2 8-12 $\mu\text{m}$ source

The 8-12  $\mu\text{m}$  supercontinuum (SC) source is currently under development by DTU and in its final stage. We have proposed and implemented a so-called cascading scheme to achieve long-wavelength (LW) mid-infrared (MIR) SC generation starting from a near-infrared 1550 nm seed. Figure 21 below shows the block diagram of the proposed and implemented architecture for the 8-12  $\mu\text{m}$  SC source after DTU restarted with FLAIR.

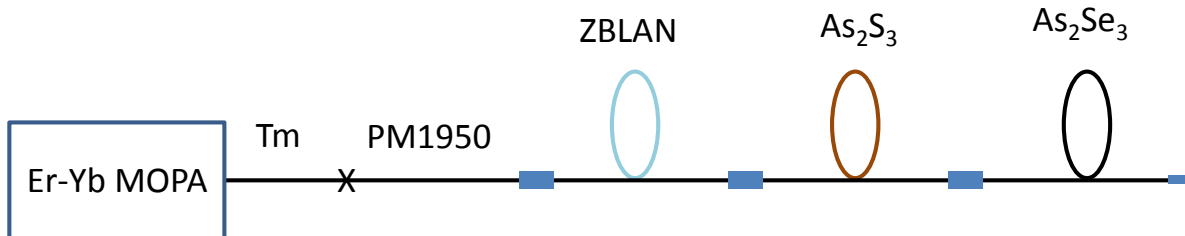


**Figure 21 : FLAIR LW-MIR SC architecture.**

First, in order to investigate the feasibility of the proposed scheme we have made an experiment with an already existing in-house made Er-Yb doped master oscillator power amplifier (MOPA). The MOPA is seeded by a directly modulated laser diode emitting at 1556 nm wavelength, which has a fixed pulse width of 1 ns, and a repetition rate that could be varied from 10 KHz to 20 MHz. The seed signal was amplified in three stages. The first two stages use an Er-doped fibre, and the third stage has an Er-Yb-doped fibre, in order to increase the absorption at the pump wavelength. The core diameter of the Er-Yb-doped fibre in the final stage was limited to 10  $\mu\text{m}$ . The peak power in the final stages crosses the kilowatt (kW) level. The small core diameter of the fibre leads to very high power density and enables crossing of the threshold level of nonlinear effects. This leads to in-amplifier SC generation up to  $\sim 2400$  nm. A piece of Thulium (Tm) doped fibre is then spliced to the output fibre of the MOPA, which acts as a red-shifter and extends the spectrum further up to  $\sim 2800$  nm. The Thulium doped silica fibre absorbs in the wavelength region of 1.5-1.8  $\mu\text{m}$ , and therefore it acts as an important isolator to avoid damage to the MOPA from any back-reflections. In order to mode match and improve the coupling efficiency to ZBLAN fibre, a short length of PM1950 is spliced to the Tm doped fibre and the other side is connectorised and polished for easy coupling to the next non-linear fibre in the cascade system.

All the three nonlinear fibres, the  $\text{ZrF}_4\text{-BaF}_2\text{-LaF}_3\text{-AlF}_3\text{-NaF}$  (ZBLAN) fluoride glass fibre, the Arsenic trisulfide ( $\text{As}_2\text{S}_3$ ) fibre, and the Arsenic triselenide ( $\text{As}_2\text{Se}_3$ ) fibre, are connectorised with FC connectors and polished in order to realise a cascading system with minimum coupling loss. Once all fibres are connectorised and polished the output of the PM1950 fibre is connected to the ZBLAN fibre, which broadens the spectrum past 4  $\mu\text{m}$ . The output of the ZBLAN fibre is then connected to the  $\text{As}_2\text{S}_3$  fibre, which further pushes the spectrum beyond 6.5  $\mu\text{m}$ . Finally the output of the  $\text{As}_2\text{S}_3$  fibre is pumped into the  $\text{As}_2\text{Se}_3$  fibre, which extends the spectrum up to 10  $\mu\text{m}$ . Figure 2 shows the broadest spectrum obtained, which span from 1.7-10  $\mu\text{m}$  with average output power of 50 mW. This spectrum is obtained at 2 MHz repetition rate and 1 ns pulse width of the seed.

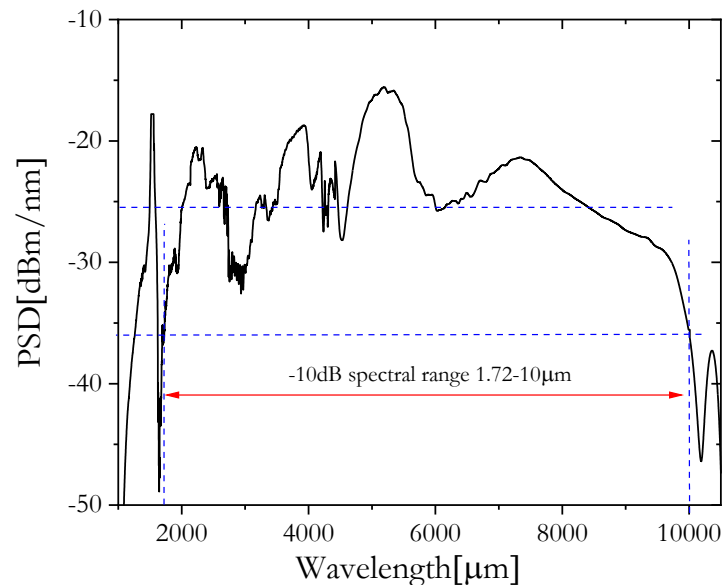


**Figure 22 : Measured output spectrum of the FLAIR 1.72-10  $\mu\text{m}$  supercontinuum source.**

The specific design of the pump and fibre cascade is highly non-trivial and has required a lot of iterations to converge towards the optimum combination of the length, numerical aperture, and core diameter of the individual fibres. The Tm-doped fibre and the mid-IR ZBLAN and chalcogenide fibres are very expensive, costing more than \$500 per meter, so the development could first start once DTU received the funds from FLAIR that was for a long time held back by former project coordinator Tekever.



**Figure 23 : Packaged LW-MIR FLAIR supercontinuum source in a 474 x 300 x 134.5mm box.**

Once the feasibility of LW-MIR SC generation was tested on an optical table we started designing and implementing both the electronics and optics of the source to make it compact and portable, e.g., not requiring an external pulse generator. Currently all the electronics and optical components are packaged and tested in a 474 x 300 x 134.5 mm box and we are working on packaging of the nonlinear fibres in the same box, which is challenging as the fibres are very soft and fragile and need proper cooling. Figure 3 shows the packaging box, in which the electronics and the optical systems are integrated. Based on the request of the RU we interfaced the packaging with a BNC connector synchronization signal output to make lock-in detection during measurements. And also an extra BNC connector is also interfaced BNC connector if desired. A complete long term power and spectrum characterisation will be made once everything is inside the box before shipping the source to RU.

## 5.2 Multipass cell

In December 2018 a first prototype was sent to CSEM for initial evaluation and design feedback. Thereafter, the mirror reflectivity study reported earlier on different mirror coatings from different mirror suppliers was extended by two more commercial mirror candidates. We found that protected Au mirrors from EKSMA clearly has the best reflectivity (~99%) and will be used for FLAIR. This will allow for around 20 m path length before the cell transmission is expected to be reduced to below 50%.

A gas cell thermos enclosure around the multipass cell kernel was investigated in detail and re-designed for fast gas exchange. A gas flow of 1-2 litres per second is required to achieve the time resolution set in the system specification. A suitable rotary pump was selected for this task. The challenge then was to balance the air flow in a stable manner in a transverse gas flow through the cell along the entire cell length. A binary split tree of air tubes into the multipass cell was found to be a good sample air delivery system, which was demonstrated in the April 2019 technical meeting in Neuchatel.

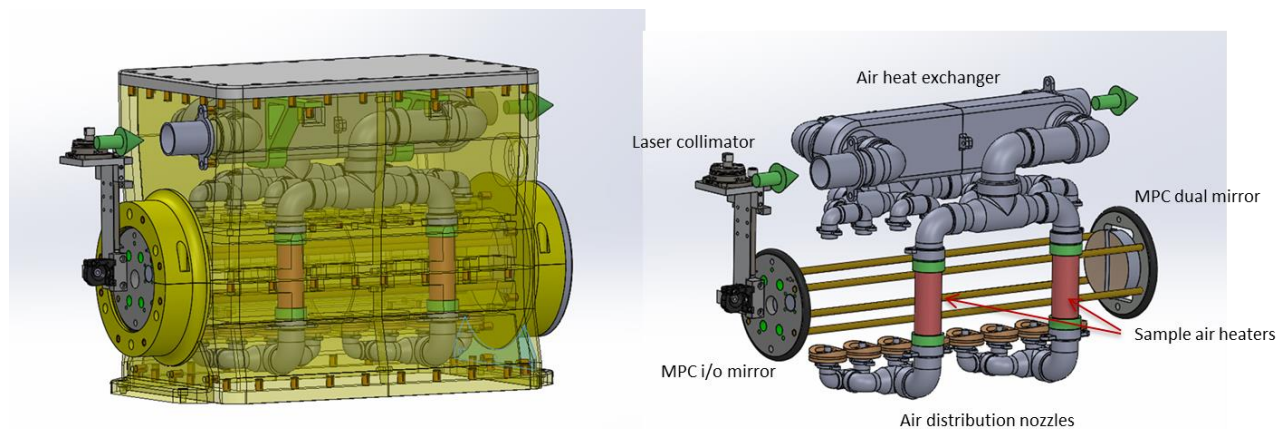


**Figure 24 : The multipass cell with thermos system (right), and sub systems (left).**

The multipass cell design regarding convenient and stable interface with the subsystems T4.1, T4.3 and T4.4 was discussed in the project, and agreed upon. A new multipass cell, based on the final choice of mirrors and system interface was designed, produced and inserted into the final thermos prototype, which now included a number of thermistors, internal heaters and fans to actively control the thermos internal temperatures. This is to assure a stable operation temperature to gain optimum cell transmission stability during flight, when ambient temperature may rapidly change. To avoid cooling down of the thermos due to the large flow rate of sample air, an inlet air temperature sensor and air heaters were also introduced to the thermos air handling system. In addition, to reduce the power consumption of the air heaters, a heat recovery module was designed where the inlet air gets preheated by the warm exhaust air. This work actually belongs to T4.3 Gas Handling System, but for practical reasons was carried out by Senseair and integrated in the multipass cell (T4.2).



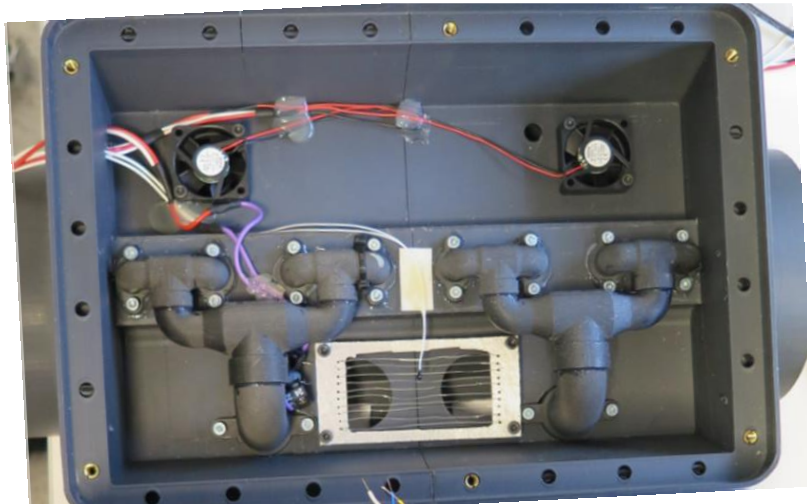


Figure 25 : The multipass cell thermos with two fans (on upper half) for inner closed space air circulation, and heater with thermistor (on lower part) for thermos temperature regulation.

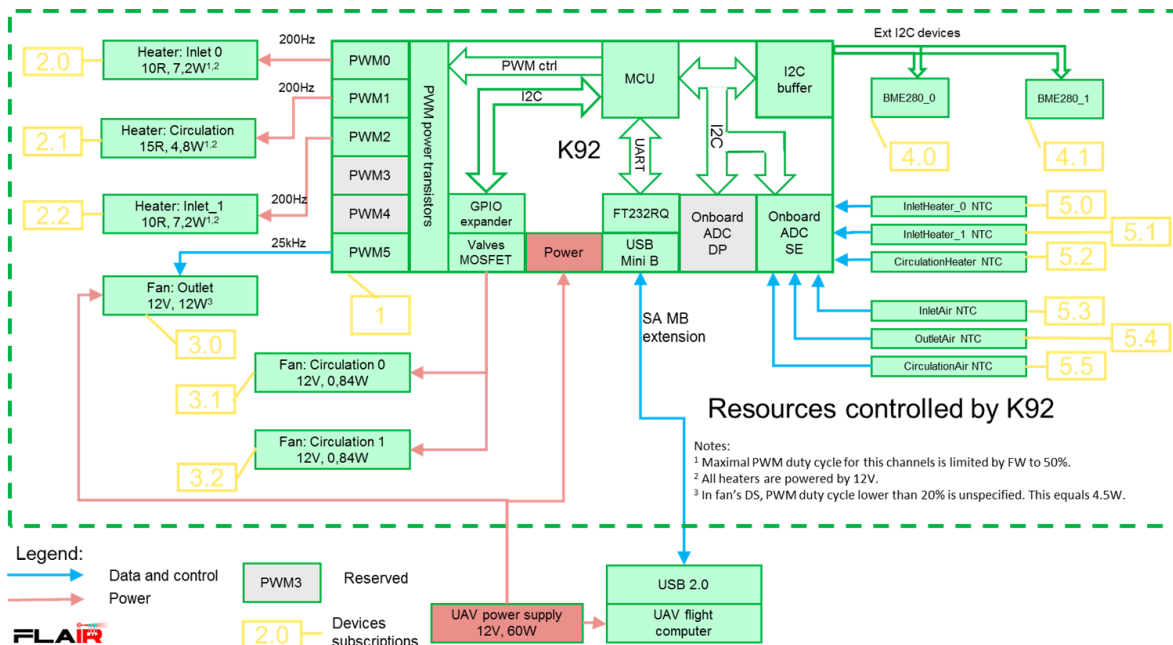
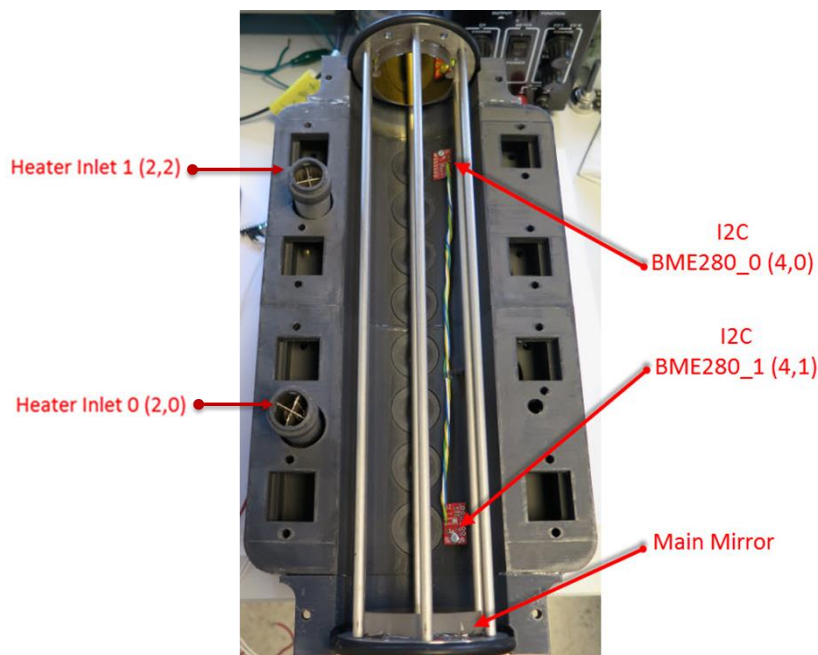


Figure 26 : The multipass cell system control block diagram.

Two extra sensor modules were assembled in the center of the multipass cell volume that measure sample air temperature, pressure, and relative humidity. This information is required to fully interpret the spectra recorded during flight, and the ultimate measurement results. In order to monitor all sensing elements inside the multipass cell system, as well as to manage and configure the multipass cell pump rate and temperature settings, a special control system was developed and connected to the thermos housing.



**Figure 27 : Location of T/P/RH sensors in the inner optics chamber (BME280).**

This first complete multipass cell system was delivered to CSEM in October 2019 for integration and test. Based on the feedback to come, a final multipass cell system will be produced and delivered to CSEM before the end of this year.

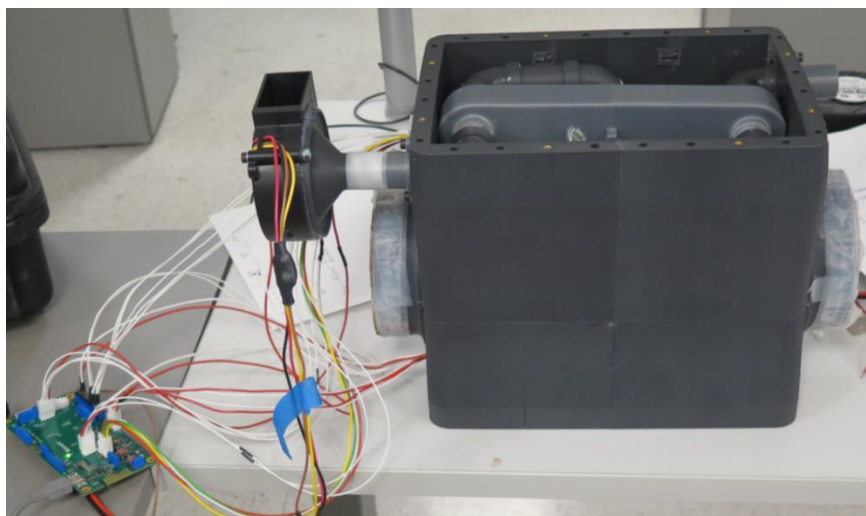


**Figure 28 : The current multipass cell prototype with fan, and control card connected with wires.**

### 5.3 Gas Handling System

Before becoming an integral part of the multipass cell and is described in the previous subsection, several tests have been performed on the first MPC version delivered by Senseair.

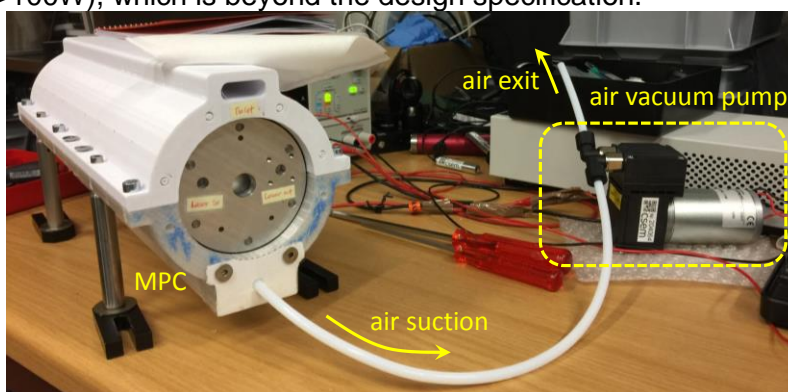
#### 5.3.1 Multipass cell gas handling system

Two different methods to circulate the ambient air into the gas multipass cell (MPC) were evaluated: the first one using a vacuum pump, as recommended by a partner using a similar setup on a tramway, and the other using a fan. However, notice that this test cell provided by



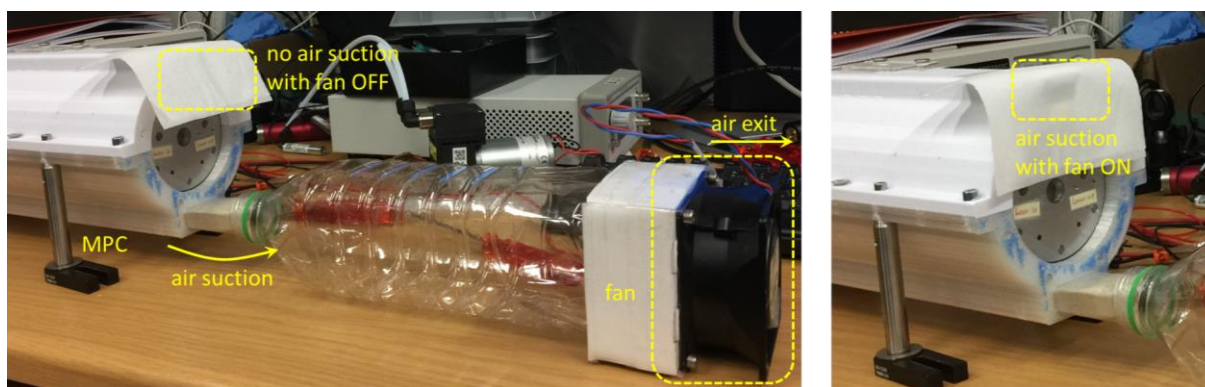
SenseAir was not yet sealed. So, it was difficult to quantitatively evaluate the performance of these two methods. But, it was enough to validate if a fan could be implemented as an efficient air circulation tool for higher air throughput through the MPC.

Figure 29 depicts the air circulation setup, based on a vacuum pump (model name, N86KNDC from KNF). The pump capacity is 6 liter/min (equivalently 0.1 liter/sec), while the volume of the MPC is roughly 0.75 liter. A light tissue was attached in front of the inlet of the gas cell. But, as expected, the air circulation was not sufficient enough to suck the tissue to the cell. KNF provides another model that has 1 liter/sec capacity, but it is 3kg and requires the high power consumption (>100W), which is beyond the design specification.



**Figure 29 : Gas handling system for the test proto-MPC, using a vacuum pump**

However, we found that a fan could be a good solution. A PC fan (model name, PAPST 8112K) was tested. Its capacity is about 16.5 liter/sec and requires only 3W (See Figure 30). It was attached to the cell through a plastic bottle, in order to evacuate the air from the cell. Then, it was clearly see that the sufficient amount of the ambient air was entering into the cell. We didn't measure the air flow in this gas handling system, but we could decisively conclude that this method could be used as gas handling system.



**Figure 30 : Gas handling system for the test proto-MPC, using a fan**

### 5.3.2 Laboratory gas handling system

In order to evaluate the sensing sensitivity of the laboratory spectrometer, 2 different gas bottles were used: one is filled by only N<sub>2</sub> gas while the other contains 4% of CH<sub>4</sub> (the rest 96% is N<sub>2</sub>), as shown in Figure 31 (schematic diagram) and Figure 32 (experimental setup). So, simply by combining the two bottles, we could accurately adjust the CH<sub>4</sub> concentration inside the gas cell. A vacuum pump was then used to evacuate the cell, so that the gas concentration inside the cell remained constant at a desired level. The flow rate of the gas bottle could be controlled from 0% to 100% by 1% step. This way, the CH<sub>4</sub> concentration could be set from 396ppm to 40000ppm (See Table 3). Bear in mind that 396ppm is the minimum

that can be set using this configuration. Recently, we bought a new gas bottle that contains only 50ppm of CH<sub>4</sub>, which will allow us to set the minimum concentration to 0.5ppm.

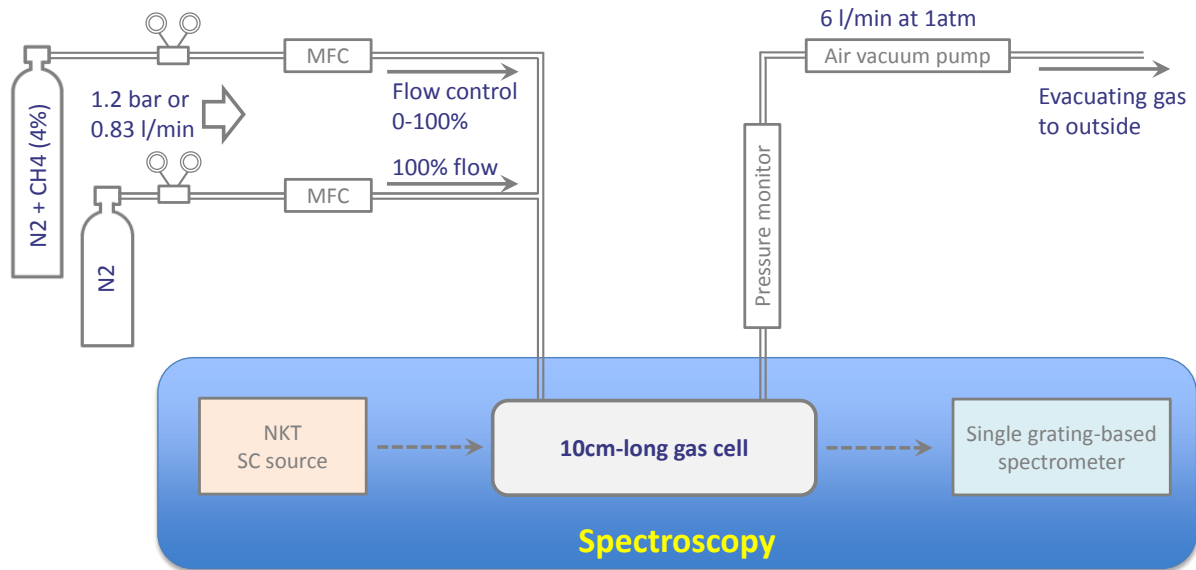


**Figure 31 : Schematic diagram of controlling the CH<sub>4</sub> concentration inside the gas cell**

**Table 3 : CH<sub>4</sub> concentration by combining two gas bottles.**

N2 bottle	N2 + CH4 bottle		CH4 in cell
N2	N2	CH4	Concentration, ppm
100	0	0.0000	0
0	96	4.0000	40000
100	96	4.0000	20000
100	48	2.0000	13333
100	24	1.0000	8000
100	12	0.4800	4286
100	6	0.2400	2264
100	3	0.1200	1165
100	1	0.0400	396

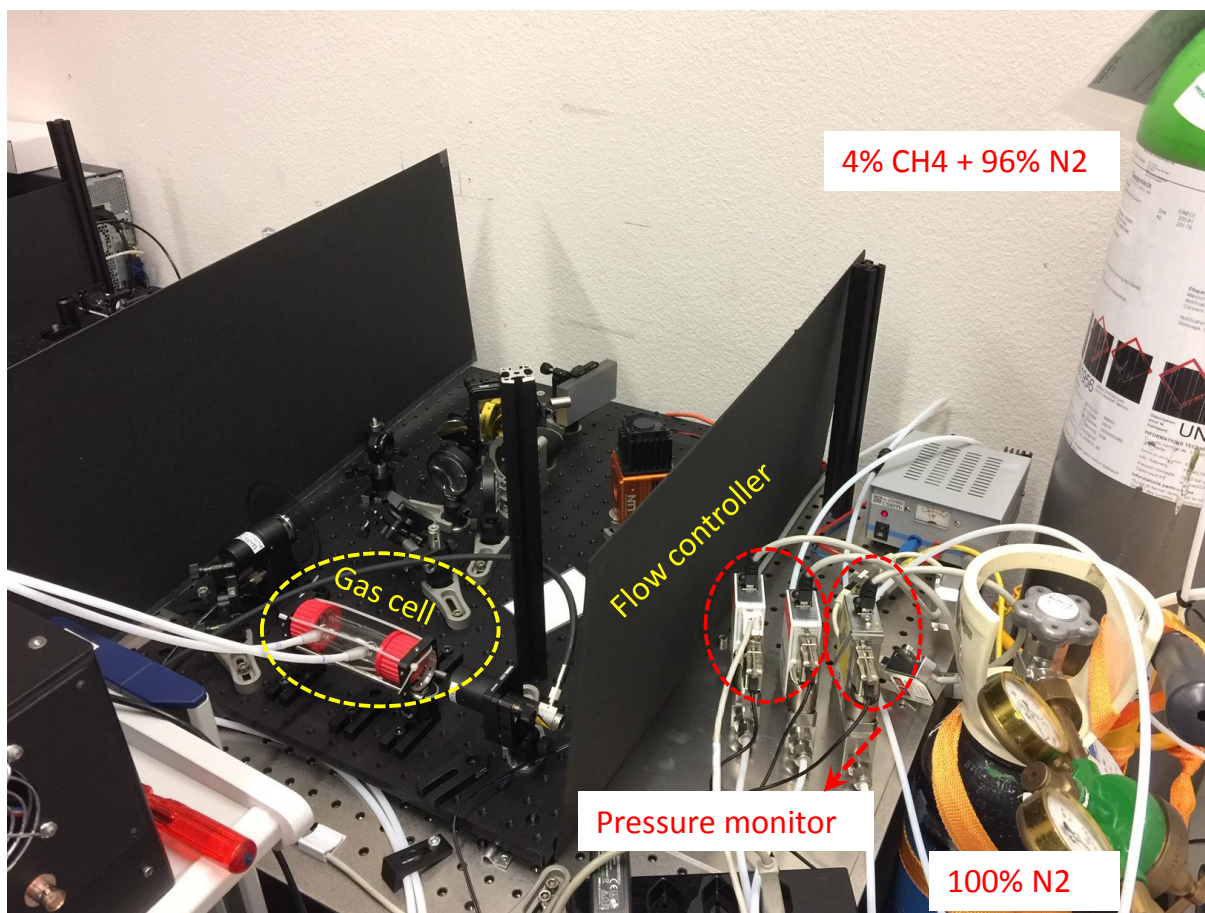


Figure 32 : Experimental setup of controlling the CH<sub>4</sub> concentration inside the gas cell.

## 5.4 2D spectrometer and imaging optics

During this reporting period, a significant effort has been placed in the realisation of the 2D spectrometer. The preliminary results of measurements performed on the laboratory spectrometer based on the VIPA dispersive element have shown a SNR level incompatible with the needs of the project partners. Alternative spectrometer designs have been identified, assembled, and tested.

Finally the decision to abandon the VIPA approach and the selection of the spectrometer design to be assembled for the FLAIR flying prototype has been validated during the consortium meeting held in Neuchâtel in April 2019. The consortium decided to target CH<sub>4</sub> absorption, with a single grating, possibly placed on a motor for extended coverage, and use the NIT camera developed within the FLAIR project as a detector.

The following section summarize the work done on the different types of spectrometer, and the effort towards integration of the flying prototype.

### 5.4.1 Laboratory setup

The different types of spectrometer have been modelled in Zemax, whenever needed, and then assembled on our optical tables for testing their real performances.

#### 5.4.1.1 VIPA based spectrometer

The baseline of the project was to use a cross-dispersed spectrometer to produce 2D absorption spectra on the 128 x 128 NIT camera. The laboratory version of the VIPA based 2 dimensional spectrometer, as pictured in Figure 33, has been already presented in the



previous periodical report. It is composed of the SC source (NKT, first delivered MIR system) connected to a mirror based collimator (Thorlabs RC04APC-P01), followed by an optical bandpass filter (e.g. IWPB3700-4500). The purpose of the filter is to narrow the optical spectrum to avoid overlapping of modes on the detector, and to absorb the remaining seed laser at  $1.6 \mu\text{m}$ . The gas cells can then be placed on the collimated portion of the beam. Alternatively, additional mirrors can be placed to direct the light towards the MPC, once it will be delivered. A cylindrical lens (Thorlabs LJ5027RM-E) focusses the beam on the VIPA (Lightmachinery, Inc. OP-7553-3000-1 Rev A). A portion of the vertically dispersed light is then dispersed horizontally by a ruled reflective diffraction grating (Thorlabs GR2550-30035). A metallic off-axis parabolic mirror (Thorlabs MPD2151-M01) images the 2D dispersed spectrum on the NIT PbSe Camera developed within the frame of the project.

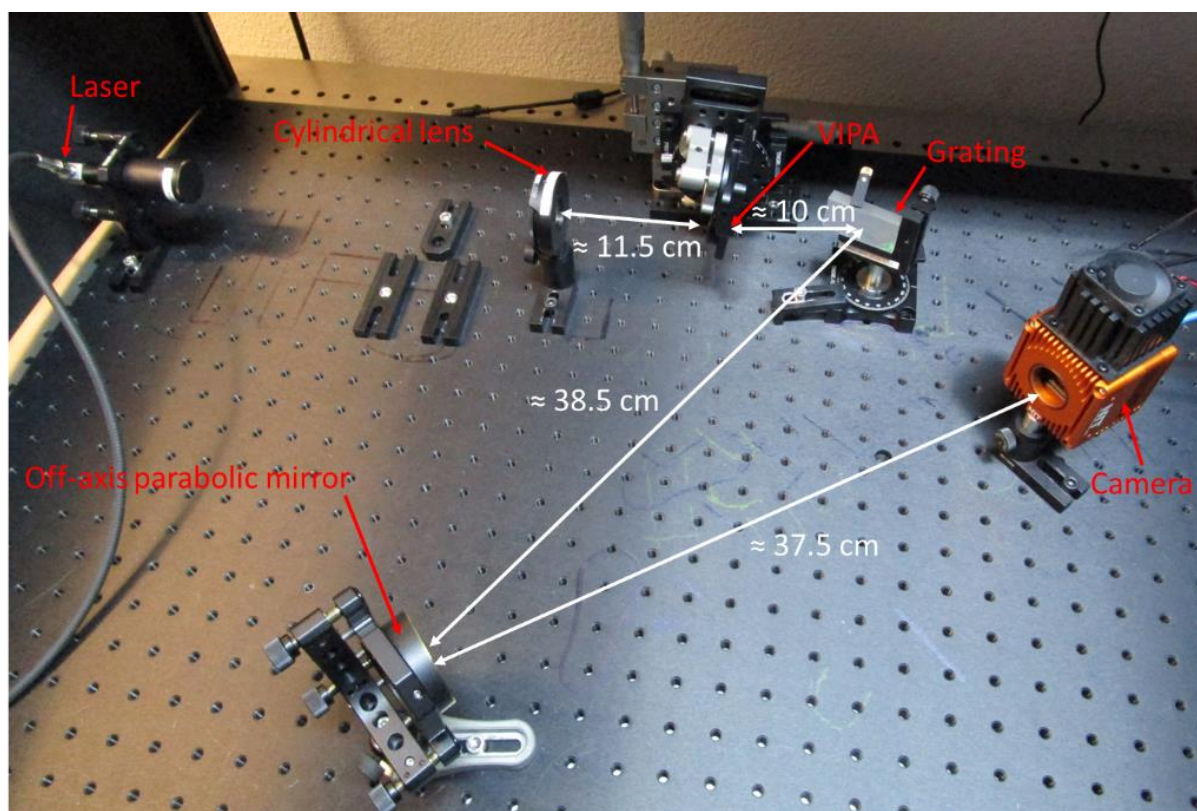
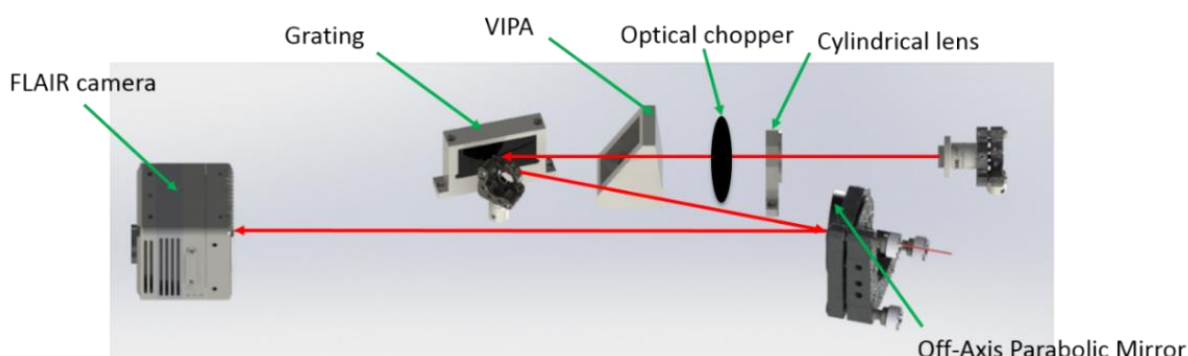


**Figure 33 : VIPA based 2D spectrometer setup. (top) sketch (bottom) laboratory realization.**

Additional work has been performed during this reporting period to understand the limits of this implementation and to increase the SNR of the system. Absorption measurement performed on 10 cm long  $\text{N}_2\text{O}$  and  $\text{CH}_4$  reference cells with various pressures, and extrapolated to a lossless, 10m long path length, indicate a detection limit between 100 and 250 ppm for  $\text{N}_2\text{O}$ , and above 5000 ppm for  $\text{CH}_4$ . The detection limit for methane has been estimated in a spectral

region where methane and nitrous oxide have overlapping absorption spectra, but away from the Q-branch. The detection limit might be slightly improved (up to a factor 10) when targeting the 3.3 $\mu$ m region, but remains some orders of magnitude too high for testing the prototype in outside environmental conditions.

The spectral coverage (35.1  $\text{cm}^{-1}$ ) and resolution (0.1 $\text{cm}^{-1}$ ) have been estimated based on HITRAN simulations (see Figure 34) and are within specifications.

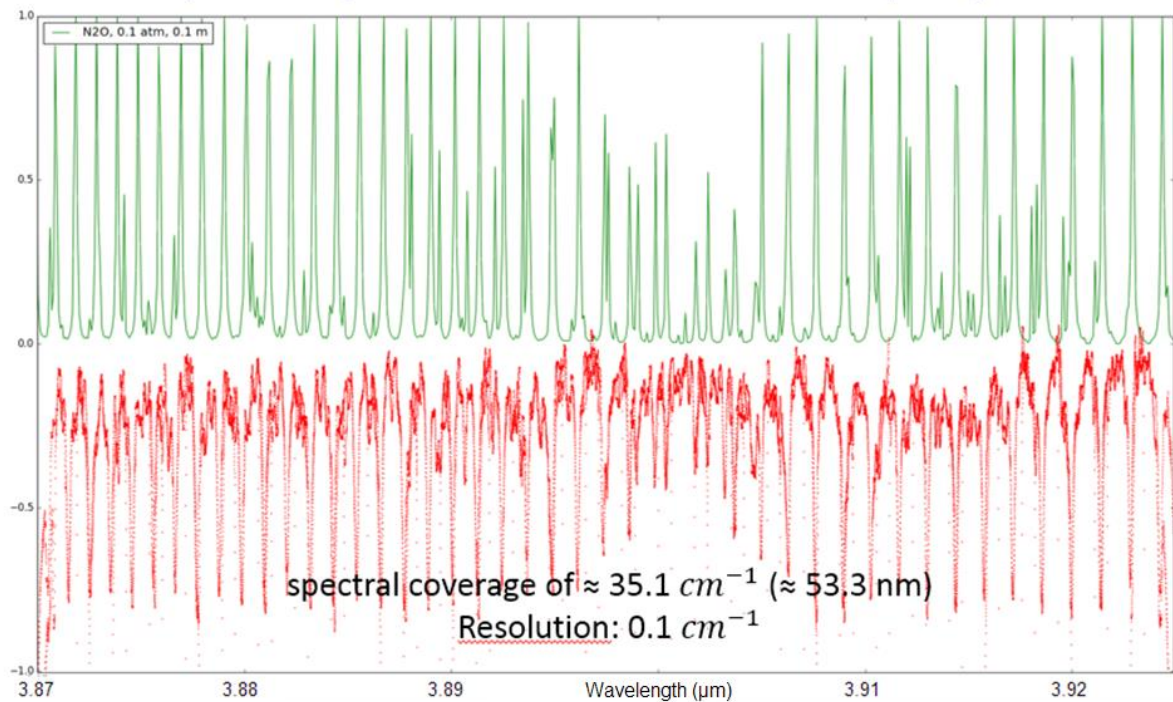


**Figure 34 : Comparison between HITRAN simulated absorption spectrum (top, green) and actual measurement on N2O reference cell (bottom, red) indicate a spectral coverage of 35.1  $\text{cm}^{-1}$  and spectral resolution of 0.1  $\text{cm}^{-1}$ .**

Such absorption spectra are extracted from the 2D dispersion pattern as recorded by the NTI camera (Figure 35, left), where each off vertical line corresponds to a portion of the spectrum. Figure 35 (right) illustrates how the final linear spectrum is obtained by containing several of those lines. The 2D spectrum optimally fills the 2D detector array, with some redundancy, and no unused pixels.

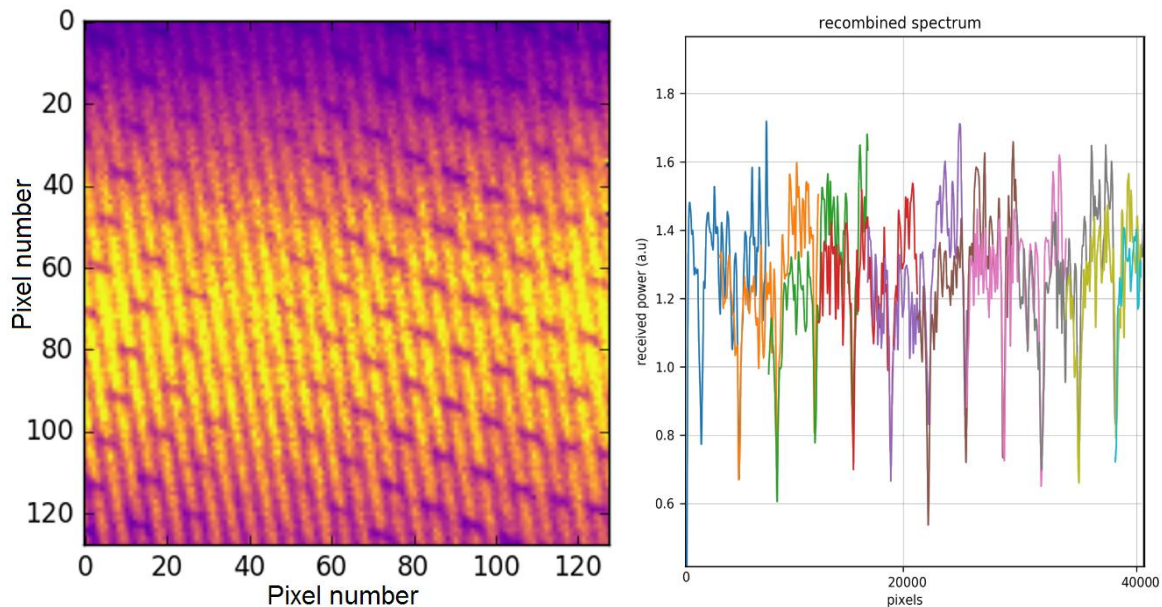


Figure 35 : (left) example 2D absorption spectrum of  $N_2O$  recorded on the NIT camera, and (left) linearization of the 2D spectrum line by line, with each line shown in different color for clarity.

#### 5.4.1.2 Crossed-grating based 2D spectrometer

Due to the limited sensitivity of VIPA-based spectroscopy, CSEM decided to construct another 2D spectrometer, which makes use of the combination of one echelle grating and one normal grating, as shown in **Error! Reference source not found.** (schematic diagram) and Figure 38 (experimental setup). The principle of this echelle grating-based spectroscopy is very similar to the VIPA-based one. An advantage of echelle grating over the VIPA, in addition to the ease of alignment, is the smaller optical power loss; hence leading to a better signal-to-noise ratio, but it is at the cost of slightly larger spectral resolution.

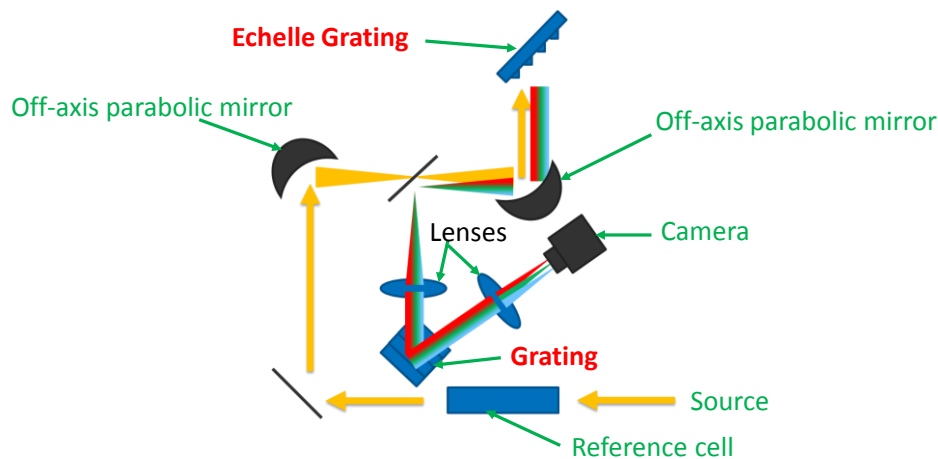
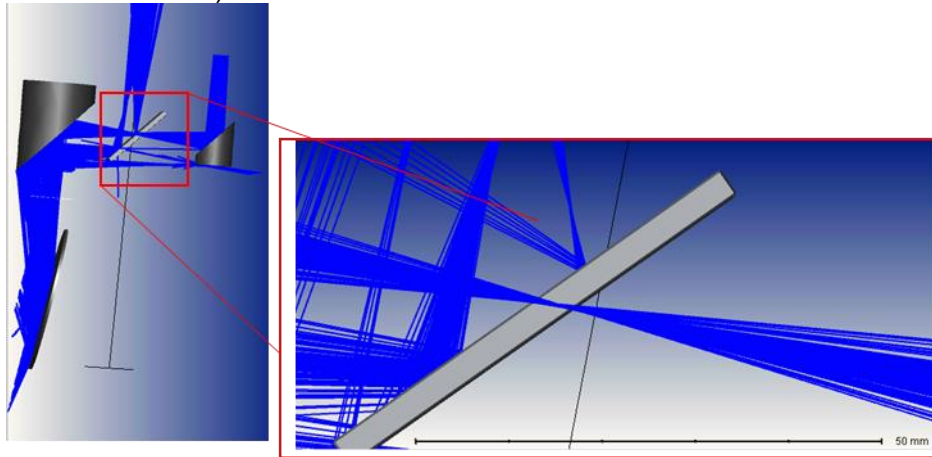


Figure 36 : Sketch illustrating the working principle of the crossed-grating 2D spectrometer.

Figure 36 shows a sketch and the Zemax model of the version implemented at CSEM: The beam coming from the multipass cell is collimated, before being focused by a  $90^\circ$  off-axis parabolic mirror, re-collimated by a second  $90^\circ$  off-axis parabolic mirror and finally directed to the Echelle grating. The grating is illuminated in Littrow configuration to minimize losses, meaning that the diffracted light travels exactly in the opposite direction of the incoming light. The specific mirror configuration has the advantage that the diffracted light can easily be extracted close to the focus point of the off-axis mirrors by placing a flat  $45^\circ$  mirror right next



to the focus while slightly rotating the grating around its surface normal. Mirrors and grating have been chosen such that at least 2 orders of the central wavelength are extracted (see zoom on the Zemax model).



**Figure 37 : Zemax model used to validate the sketched concept.**

The extracted light is then collimated by a lens before being cross-dispersed by the second grating, and then focussed on the camera with the Fourier lens. The setup was assembled and aligned with a visible laser and subsequently tested with a supercontinuum from NKT.

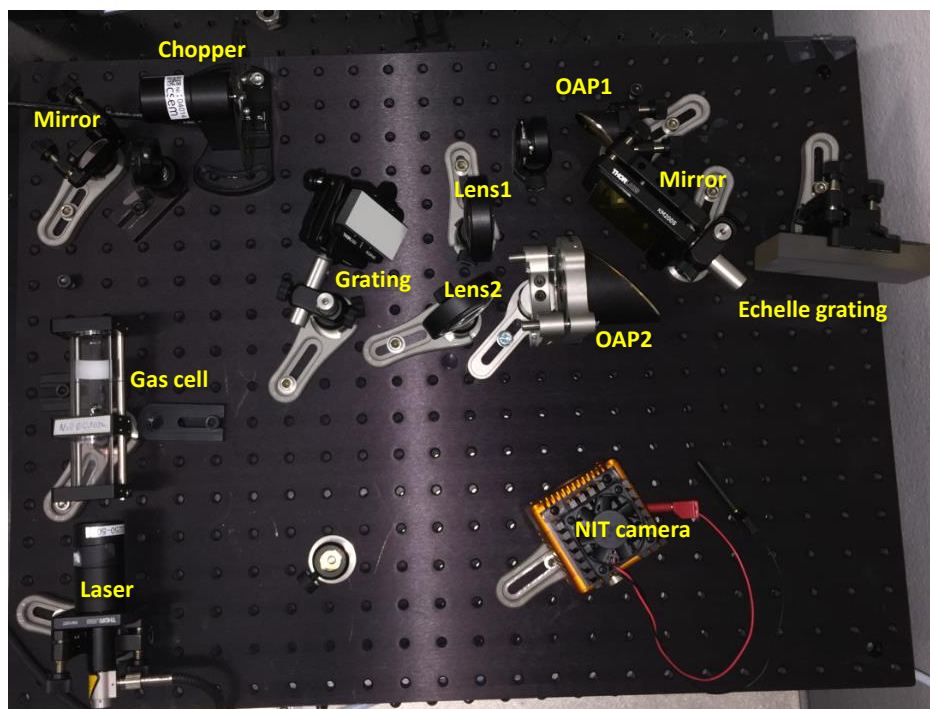


**Figure 38 : Experimental setup of 2D spectroscopy, using a combination of one echelle grating and one normal grating**

The broadband supercontinuum collimated laser passed through the 10cm-long gas cell before being expanded by the two off-axis parabolic mirrors OAP1 and OAP2. The focal point is placed just underneath the square mirror. The expanded beam hits the echelle grating. Then, the reflected light from the echelle grating (in other words, wavelength dispersed light in vertical direction) is directed to a normal grating for a further dispersion in horizontal direction. The Lens 1 serves to collimate the beam, as it has been focused again by OAP2. Finally the Lens 2 serves as a Fourier lens to resolve the dispersed light on the NIT camera. Consequently, the broadband light source turned to be spatially dispersed in 2 dimensions, which makes it



possible to perform a wide spectral range measurement, as shown in Figure 39. It is noteworthy that, in contrast to the VIPA based setup, only a portion of the camera pixels contribute to the absorption signal (compare Figure 35 and Figure 39).

We can see 6 distinct lines in y-axis. Each line corresponds to an individual transmission spectrum at different wavelength. As clearly seen, the spectrum at pixel #48 in x-axis experienced a strong gas absorption (See the yellow dotted circle in Figure 39), which was caused by the Q-branch of Methane at around 3315nm. Then, simply by computing the logarithmic ratio of the reference transmission spectrum to the spectrum that is measured at CH<sub>4</sub> 40000ppm, the absorbance at the given gas concentration could be obtained.

To evaluate the performance of the trace gas sensing system, the transmission spectrum was measured every second as a function of CH<sub>4</sub> gas concentration from 1212ppm to 40000ppm (See Table 3). 10 consecutive transmission profiles were measured for each concentration, in order to calculate the measurement repeatability. The standard deviation out of the 10 measurements were computed to demonstrate the system performance (See Figure 40).

Let us discuss more details on the experimental results of the performance. Firstly, as expected, the measured concentration shows a good agreement with a theoretical exponential Beer-Lambert absorption curve, which proves the system linearity. Secondly, it is remarkable that the system noise was measured to be relatively small for low concentration at 1212ppm. This would correspond to a value around 24ppm for a 10 m long multi-pass cell, considering 50% power loss due to reflection on the mirrors. We believe that the sensing system would be capable of measuring much lower concentration. However, the phenomenon that the absorption is saturated at about 0.52 instead of unity is abnormal. We believe that it would be attributed to the normalization issue when the transmission is computed. It seems that the noise floor level of the detector (NIT camera) is not same with and without the presence of the CH<sub>4</sub> gas inside the cell, even though it should not be the case. Then, it might lead to an offset in the computation of the transmission profile. Yet, it must be pointed out that this is totally related to the calibration issue and this offset can be readily compensated. In addition, this offset doesn't influence the performance of the sensing system, since the measurement follows well the theoretically estimated curve.

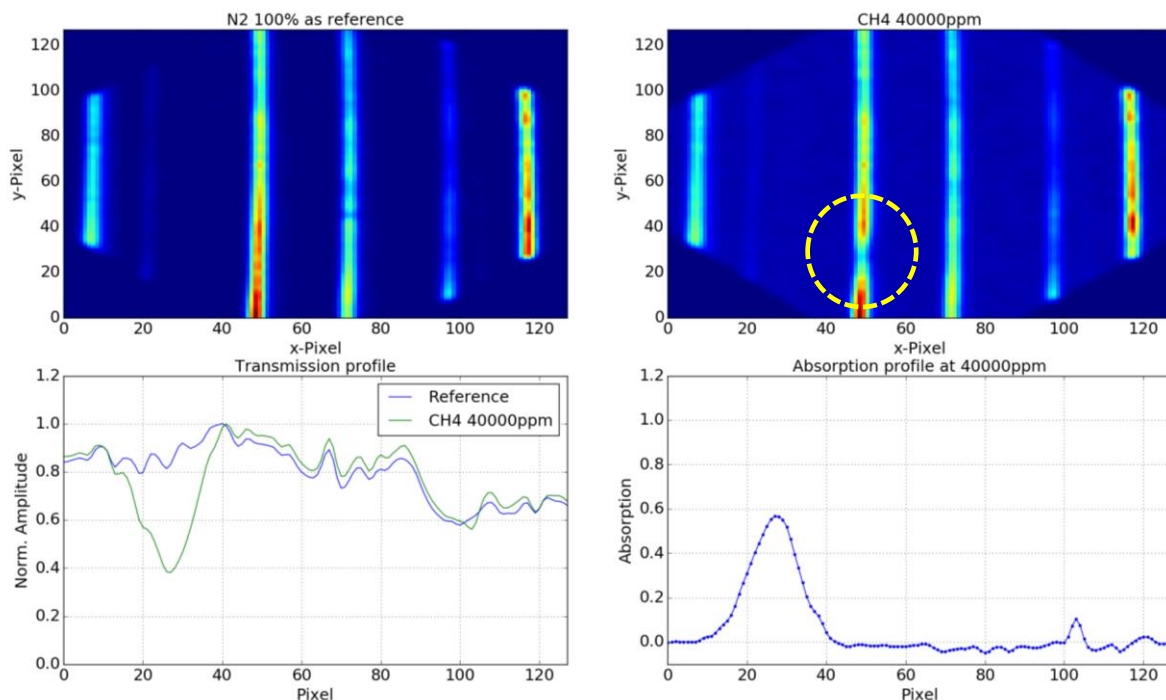


**Figure 39 : Measured CH<sub>4</sub> concentration at 40000ppm in a 10cm long cell, using echelle grating-based spectroscopy.**

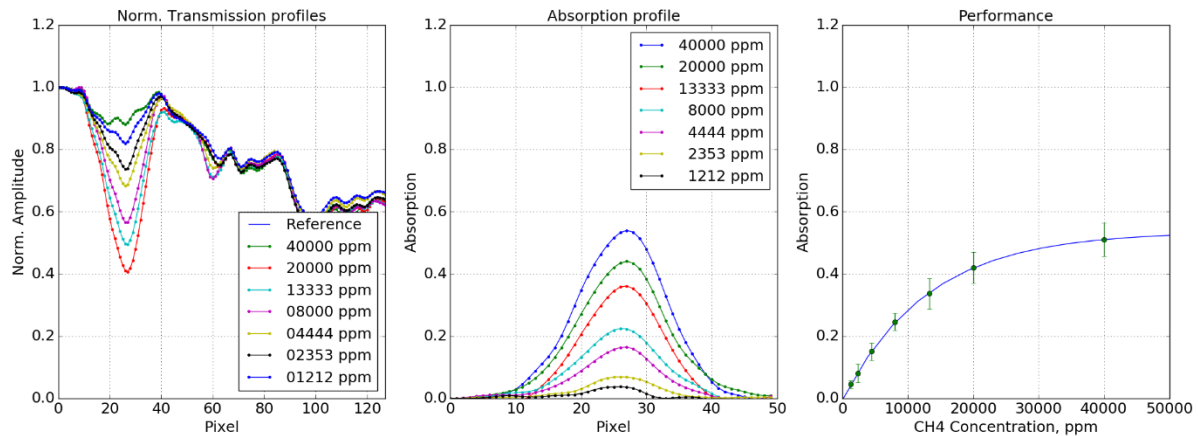


**Figure 40 : CH<sub>4</sub> absorption profiles and the repeatability for different gas concentrations.**

The spectral coverage and spectral resolution are not precisely known, since it was not possible to clearly relate each of the 8 lines on the camera to a spectral region.

#### 5.4.1.3 Prism based 2D spectrometer

Often, prisms are used as cross dispersers in application where optical power is critically low, as they reduce the optical loss, since they don't disperse to higher diffraction orders. Based on a design proposed by RU, CSEM performed some simulations to identify a suitable prism (see Figure 41)

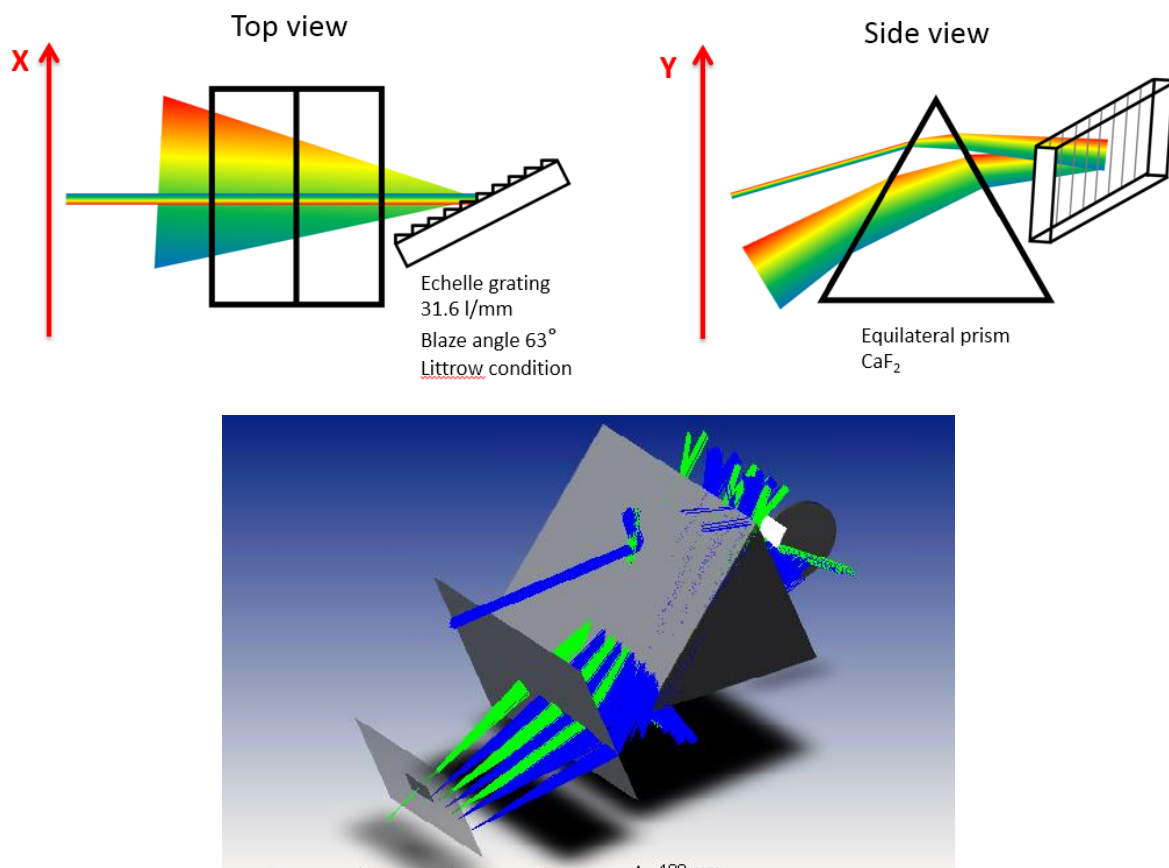


**Figure 41 : (top) schematic principle of a prism used for cross-dispersion of the absorption spectrum. (Bottom) Zemax model to evaluate the possibility to use a prism for the cross dispersion.**

Unfortunately, there are no standard materials that offer sufficiently strong dispersion (low Abbe number) in the required wavelength range. This approach has thus not been implemented by CSEM.

#### 5.4.1.4 Single grating based spectrometer – 2D 128x128 pixels detector

Echelle grating-based spectrometer could improve the sensing performance, but it was still far from the target sensing sensitivity, which is a few ppm of CH<sub>4</sub>. So, we decided to investigate another type of spectrometer, based on a single grating. Figure 42 depicts the schematic diagram of the single grating-based spectrometer. Using a focal lens (not shown in Figure 42), the supercontinuum laser beam was focused at the focal position of the off-axis parabolic mirror (OAP-1), while the 10cm-long gas cell was placed in between the laser and the OAP-1. Then, the collimated beam reflected from OAP-1 hits the grating, so that the wavelength of the light was dispersed in horizontal direction. The 1<sup>st</sup> order reflected beam from the grating was focused at the camera after being reflected from the OAP-2. Since this configuration relies on a single grating, it can be considered as 1D spectrometer.

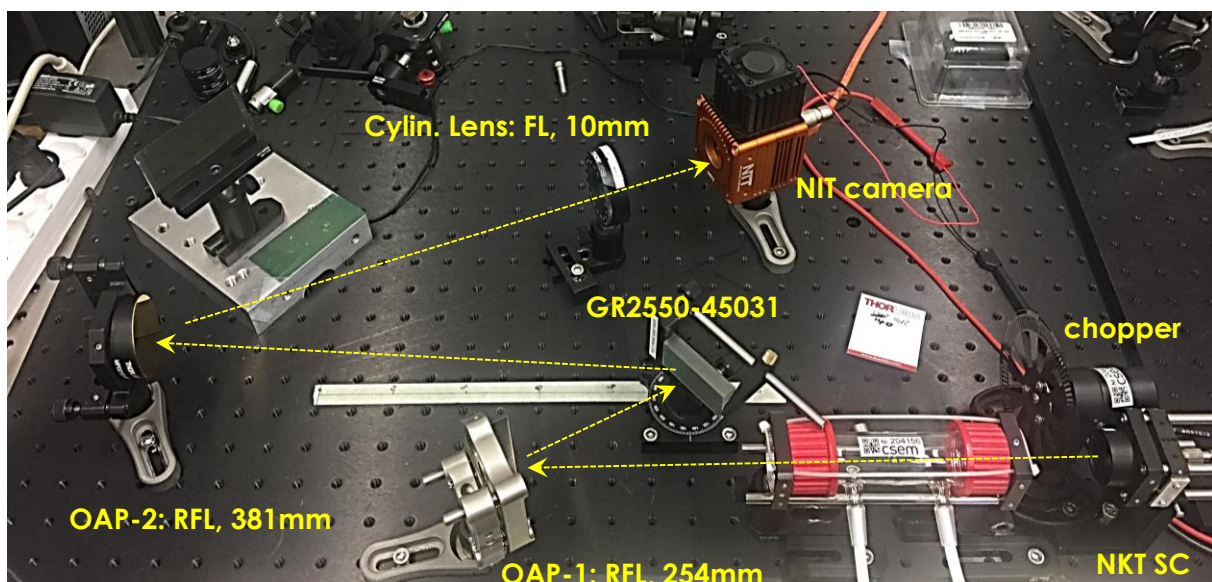


**Figure 42 : Single grating-based spectrometer.**

To take the advantage of 2D array feature of the camera, one cylindrical lens was placed in front of the camera. So, the beam was expanded in vertical direction in front of the camera. In turn, 2D image was obtained in the camera, as shown in Figure 43(left). Therefore, the x-axis of the image represents the wavelength while the y-axis of the image represents replica of the transmission spectrum.

This method has 2 crucial advantages over the other 2D spectrometers. Firstly, the optical power at the camera is strong, so the SNR of the sensing system becomes certainly enhanced. Secondly, all transmission profiles measured at each row are summed with weighting average as a final transmission profile (See Figure 59(right)). This way the inherent white noise of the sensing system and the non-uniform gain fluctuation of pixels could be significantly averaged out, resulting in the considerable improvement of SNR as well, without the need to perform NUC.

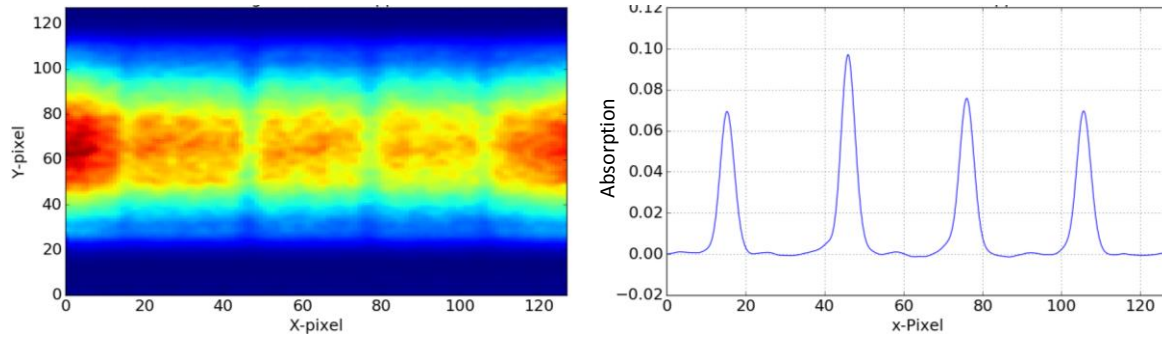


**Figure 43 : Image on the camera and CH<sub>4</sub> absorption profile at 4286ppm.**

To evaluate the sensing performance of this system, the same experiment as described in 5.4.1.2 was repeated. Figure 44 demonstrates examples of the CH<sub>4</sub> gas absorption profile at two different concentration: 1126ppm and 40000ppm, showing a good SNR. Using HITRAN simulation, the x-axis of the camera image was calibrated to wavelength.

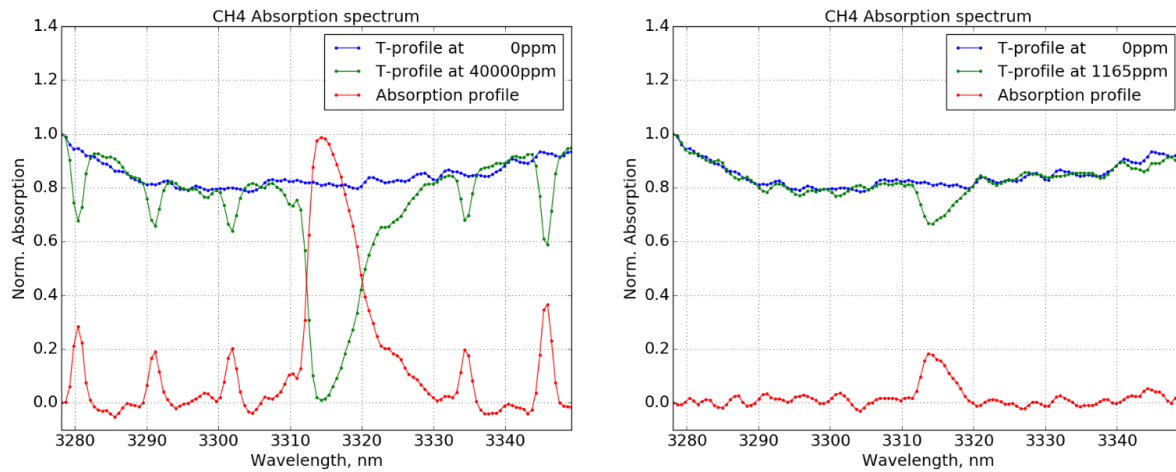


**Figure 44 : CH<sub>4</sub> concentration monitoring at 1165ppm and 40000ppm.**

Figure 45 illustrates clearly the generic characteristics of the system performance. The methane absorption was measured from 40000ppm down to 396ppm. First of all, the measured concentration matches well the theoretical Beer-Lambert absorption curve, which proves the linearity of the sensing system. For each set concentration, the standard deviation out of 10 consecutive measurements was computed, which is nearly constant over the whole concentration range. It implies that the system noise is linear and the sensor sensitivity is mainly limited by the system noise. In addition, the standard deviation is relatively small compared to the absorption amplitude at 396ppm, showing approximately factor of 4. So, we believe that this sensing system might have a potential of monitoring as small as 100 ppm of CH<sub>4</sub>.



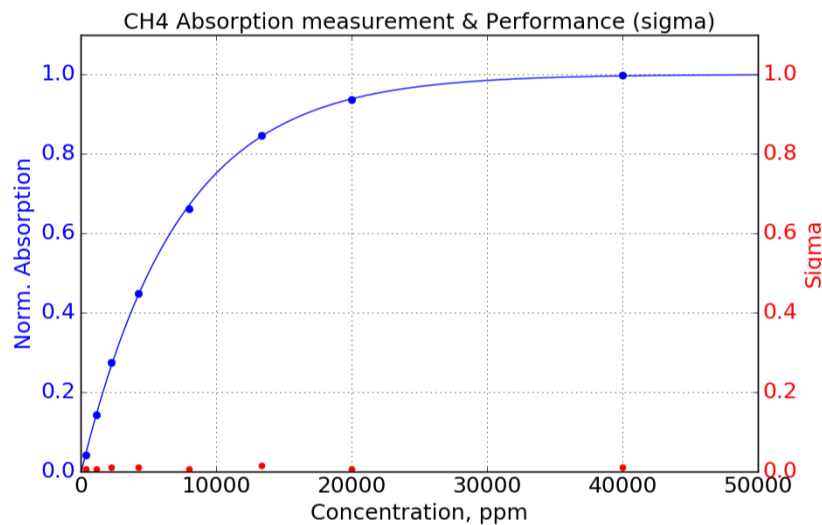


**Figure 45 : Performance of the single grating-based spectrometer.**

The CH<sub>4</sub> concentration was further reduced down to 50ppm by using only the new gas bottle. The Q-branch absorption resonance along the spectrum was measured to be clear. However, a non-negligible noise oscillation was imposed on the spectrum, which degrades the SNR to be about 3. It seems that 50ppm would be close to the sensing limit of this system for a 10 cm path length.

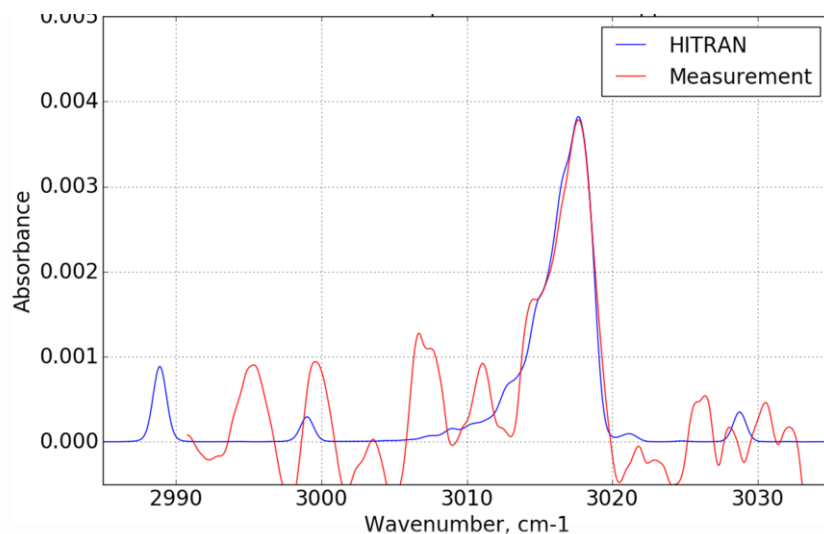


**Figure 46 : Absorption profile at CH<sub>4</sub> 50ppm with 10cm-long gas cell.**

Apart from sensing sensitivity, the spectral resolution is also important parameter for the spectrometer. Indeed, in presence of gas mixture, e.g. containing water vapor, it is important to distinguish the contribution of each components, by looking at absorption lines that are unaffected by the other gas species. Prior to the measurements, a Zemax simulation was performed, using the exact parameters of optics such as OPAs and grating (See Figure 47). So, the theoretical spectral resolution and the measurement range of the spectrometer were accurately estimated to be 0.5cm<sup>-1</sup> over 20cm<sup>-1</sup>, respectively. The absorbance at 50000ppm concentration was then measured and compared to HITRAN simulation, as shown in Figure 48. The spectral resolution and spectral range was measured to be 0.6cm<sup>-1</sup> over 18cm<sup>-1</sup> by a single shot, which matches well the Zemax simulation result. Notice that a larger spectral range measurement would be readily possible by a multiple measurement while rotating the grating angle (See Figure 42).



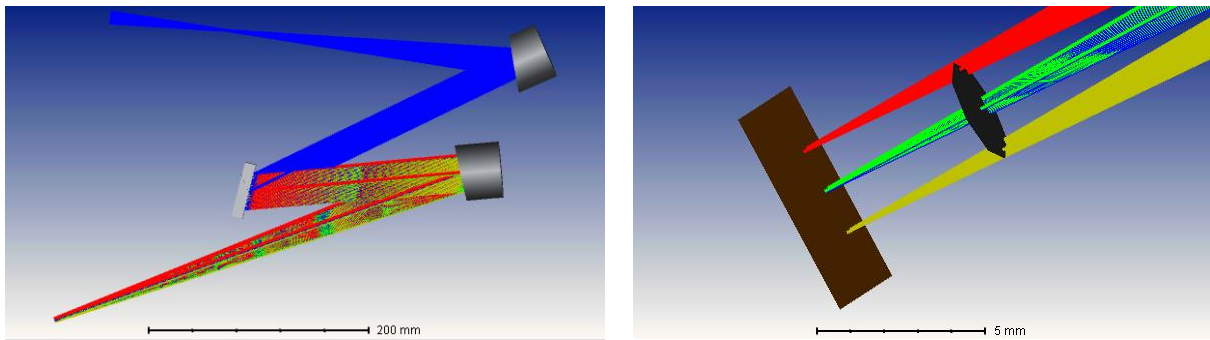


**Figure 47 : Zemax simulation to evaluate the spectral resolution of the single grating-based spectrometer**

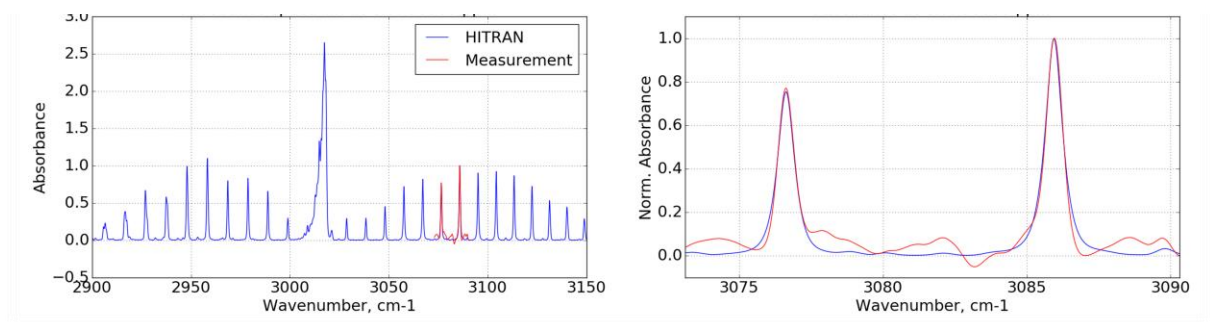


**Figure 48 : Measured spectral resolution of the single grating-based spectrometer.**

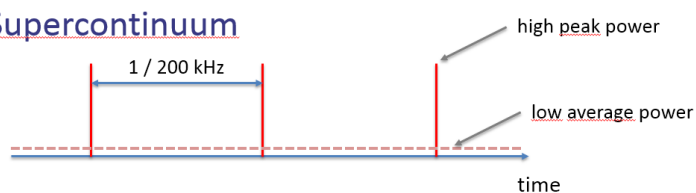
So far, all the test experiments for CH<sub>4</sub> monitoring were performed with a 10cm-long gas cell. However, bear in mind that a multipass cell should be practically utilised, which will increase the light-gas molecule interaction length to ~10m. Then, it will improve the sensing sensitivity by a factor of 100 when only considering the interaction length.

#### 5.4.1.5 Single grating based spectrometer – single pixel detector

The NIT camera suffers from non-uniformity gain across the pixels, a feature that is common to uncooled NIR detectors, and can be somewhat corrected by applying non-uniformity correction (NUC). With this in mind, we wanted test the possibility to replace the camera by a single pixel detector, and use a combination of a diffraction grating on a rotatory platform, a pinhole, and a MCT single pixel detector (PDAVJ8 from Thorlabs) to build a simplified monochromator. The setup is the same as the one shown on Figure 42, except that the camera has been replaced by the MCT detector, and that a motorized precision rotation stage (PRMTZ8/M from Thorlabs) has been used underneath the grating.

The supercontinuum light source is not continuous, but pulsed with a repetition frequency of typically 200 kHz. This means that the absorption information is contained only during high peak power pulses, thus only during a fraction of the measurement duration, and that most of the time, there is no light, which correlates with the relatively low average power of the supercontinuum (see Figure 49, left, top). Those dead times contribute to the noise of the acquired signal.

- Supercontinuum



- Detect RF harmonic of repetition rate signal

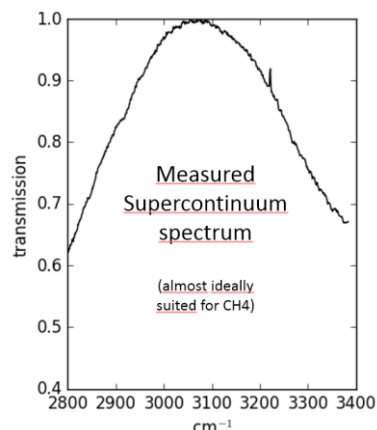


**Figure 49 : (left, top) Operation principle of the supercontinuum. (left, bottom) Working principle of the detection scheme. (right) Measured supercontinuum spectrum.**

In order to take advantage of the pulsed nature of the supercontinuum, the output signal of the MCT detector has been fed to a RF signal analyser, where the supercontinuum signal is seen as a series of sharp peaks with 200 kHz separation. Close to DC, the system is plagued with flicker noise, and at frequencies above 100 MHz (corresponding to the temporal bandwidth of the MCT detector), the amplitude of the peaks decreases. There are, however, some peaks that can be found between those 2 limits. An example is illustrated in green in Figure 49 (left, bottom). The RF signal analyser has a nice feature that allows to track the amplitude of a selected peak over time, in our case the 1.4MHz tone. By synchronizing the acquisition with the rotation of the motor, it is possible to obtain a good quality transmission measurement as a function of the wavelength. Figure 49 (right) shows such measurement performed on the supercontinuum light, hence confirming that its spectrum is ideally suited for CH<sub>4</sub> absorption measurement near the Q branch spectral region.

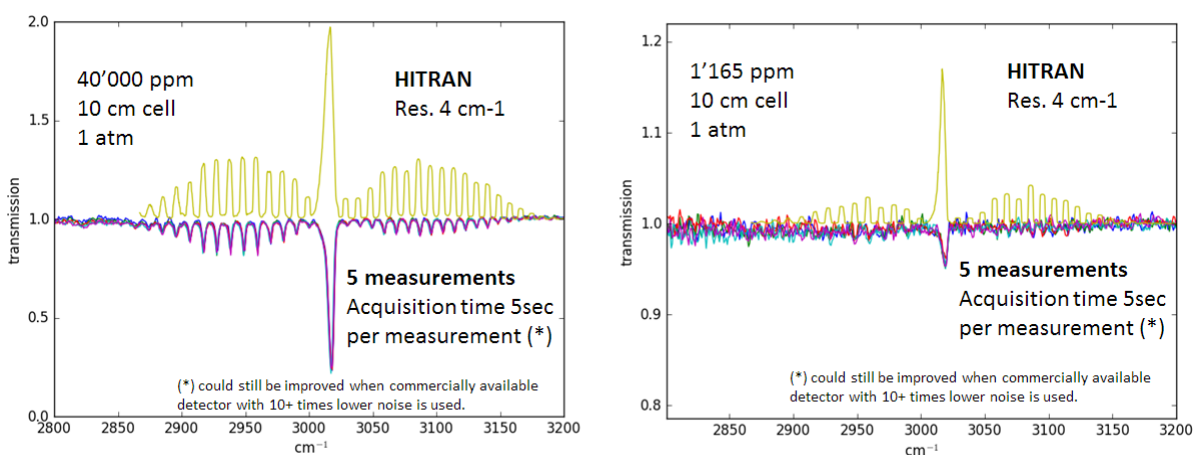


**Figure 50 : Absorption measurement through a 10 cm long cell with (left) 40'000ppm CH<sub>4</sub> and (right) 1'165ppm CH<sub>4</sub>. The bottom part shows 5 single acquisitions, and the top part the corresponding HITRAN simulation.**

Some absorption measurements have been performed on a 10 cm long cell filled with different partial pressure of CH<sub>4</sub> in N<sub>2</sub>. Two examples for 40'000 ppm and 1'165 ppm are reported in Figure 50, where the motor rotation was set to cover the 2800 to 3200 cm<sup>-1</sup> range in approximately 3 seconds. In this case, the spectral resolution has been estimated to be below 4 cm<sup>-1</sup>, and the spectral coverage 400 cm<sup>-1</sup> around 3000 cm<sup>-1</sup>. Those values may be optimized by varying the size of the pin-hole in front of the detector, or increasing the distance between the grating and the single pixel detector. A portable setup could be arranged by replacing the

RF spectrum analyser with a down-conversion mixer, or performing FFT analysis of the temporal acquisition trace.

#### 5.4.1.6 Up-conversion spectrometer

In parallel with the laboratory testing of the different solutions presented above, alternative backup solutions have been envisaged, with the goal to have a flying prototype demonstrating the capabilities of the different building blocks developed within the FLAIR project, should the FLAIR spectrometer fail to reach the objectives.

The NLIR Company has been approached, and fruitful discussions and exchanges of information happened. They provide up-conversion spectrometer that were compatible in size, weight and electrical consumption with the flying prototype constraints (see Figure 51), except maybe for the spectral resolution that is a bit high to distinguish overlaps between some gas absorption line and water. Though the extended spectral range could alleviate this issue.

Specifications	
Spectral range	3.0 – 5.5 $\mu\text{m}$
Resolution	8 $\text{cm}^{-1}$
SNR @ 1 s	~ 8.000 (up to 20.000)
Integration time	~ 1ms
Other	uncooled, vibration tolerant
Size	70 mm $\times$ 230 mm $\times$ 260 mm
Weight	5.2kg
Power supply	12V, 50W
Interface	Win10, compatible Raspberry Pi

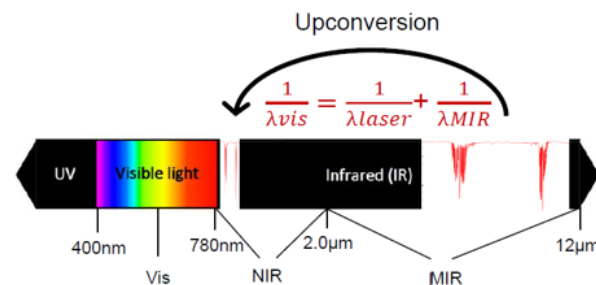


**Figure 51 : Specification table for the NLIR 3055 up-conversion spectrometer, and schematic working principle.**

#### 5.4.2 Consortium decision

The different approaches presented in section in sections 5.4.1.1 to 5.4.1.6 have been presented by CSEM to the different partners during the consortium meeting held in Neuchâtel in April 2019.

The consortium decided to drop the baseline approach with the VIPA for the following reasons: too high detection limit, low reliability of the VIPA coating (which delaminated on one exemplar under normal laboratory conditions), and sensitivity of the alignment. The other cross-dispersion approaches have also been rejected, mainly due to improper coverage of the detector array, complexity of alignment, and potential stability issues under vibration with the large dimension of the Echelle grating. The up-conversion spectrometer has been disregarded, as it doesn't fit well in the project ecosystem, and would mean abandoning the camera developed for FLAIR.

The spectrometer based on the constantly rotating motor and MCT single pixel detector has been discarded: it would not make use of the FLAIR camera, and the flying environment (accelerations, vibrations) could impair the correct operation of the motor, leading to imprecise referencing of the wavelength axis.

Finally, the single grating based spectrometer with the 2D – 128  $\times$  128 pixels detector camera developed for FLAIR has been selected. The preliminary measurements showed both an encouragingly low limit of detection, acceptable spectral coverage and compatible spectral resolution. Moreover, the idea to spread the light vertically and perform averaging over the vertical pixel columns to overcome the non-uniformity issues of this kind of detectors has been regarded as particularly elegant.

It has also been decided to equip it with a motor to extend the detection range to match the broad supercontinuum spectrum, and allowing the detection of a larger number of gas species.

Methane has been confirmed as the target gas for the demonstrations, with absorption measurements near the Q-branch.

### 5.4.3 UAV compatible setup

The UAV compatible setup has been based on the laboratory setup. During the period following the consortium meeting, some improvement – described in section 5.4.1.4 – have been applied to the laboratory setup. It required close collaboration between the engineer working in the lab and the one performing the Zemax modelling.

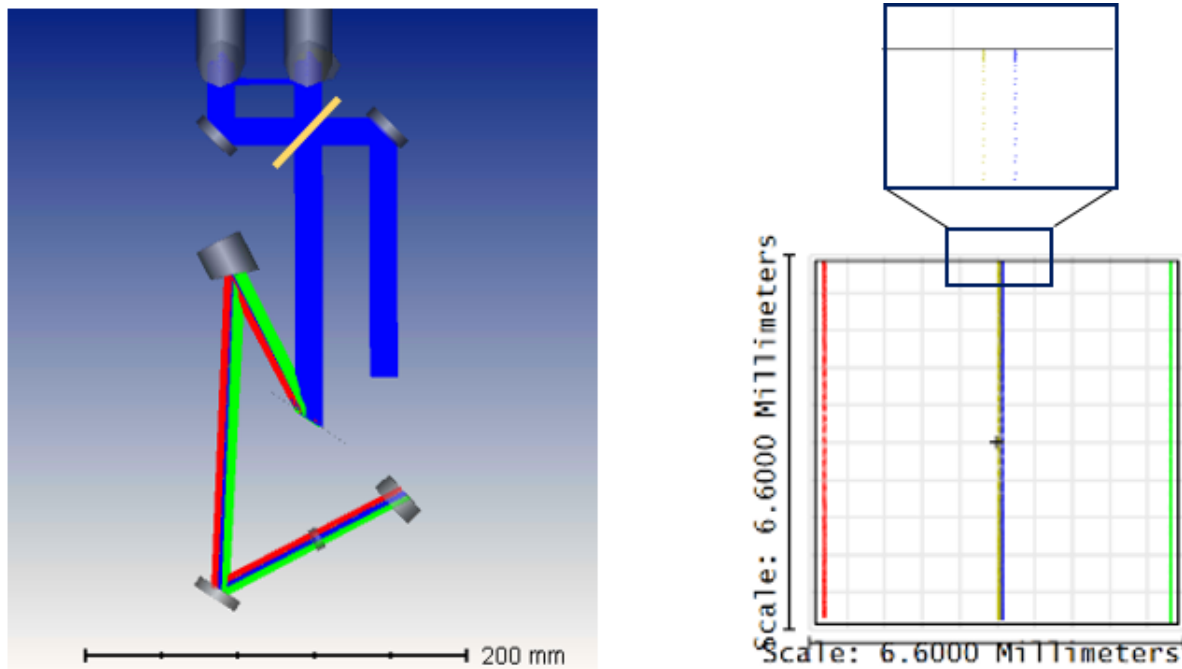


**Figure 52 : Zemax model (left) and expected resolution / spectral range on the camera detector (right) for the final design.**

In the final design, the laser light is brought to one of two identical 90° off-axis parabolic mirrors via 2 flat 45° angle mirrors. The latter allow for the introduction of a bypass mirror (marked in yellow in Figure 52) to measure the direct laser light without going through the multipass cell. The first of the 90° off-axis parabolic (OAP) mirrors deflects and focuses the light towards the entry-port of the multi-pass cell (not shown in the design), whereas the second one will re-collimate the light after the cell. According to information from Senseair, it has been assumed that the light going out of the MPC is a copy of the light entering it. The beam collimated by the second OAP goes to a 450 l/mm grating on a motorized rotating mount, which splits it into its spectral components. This spectrally diverging beam is collected by an off-axis mirror (the Fourier mirror) that focusses the spectral components to individual spots on the camera. An additional flat mirror is introduced to fold the beam path and a cylindrical lens spreads the beam perpendicular to the dispersion direction to cover the entire camera instead of only the central line. The calculated output is shown in Figure 52 right, with a central wavenumber of 3086cm<sup>-1</sup> (blue/brown). The red and green scatter lines mark the desired bandwidth of 21.3cm<sup>-1</sup> around this central wavenumber and the zoom shows clearly distinguishable lines for the desired resolution on the camera. The desired final spectral resolution is 0.5cm<sup>-1</sup>, which should ideally be covered by 3 camera pixels to clearly allow the identification of peaks. The blue and brown spots hence show this 1/6cm<sup>-1</sup> range and the measured distance on the detector is 46µm, which is in good agreement with the pixel size of the camera of 50µm. Finally, in order to shift from one spectral window of 21.3cm<sup>-1</sup> to the adjacent one, a grating rotation angle of ≈0.41° is required (depending on the exact wavenumber).

Once the preliminary Zemax modelling had been set-up, the mechanical engineer started working on the design for the assembly of the whole system, including the interface with the multipass cell. Since the mutlipass cell desing changed significantly (see Figure 53 and Figure 29), and the new model was still in fabrication, CSEM based its concept around the CAD file that had been provided by Senseair. The final design for the spectrometer was reached after several updates between optical modelling and CAD design. The reason was that going from 2 inch optics to 1 inch optics to save place and weight, or modifying the position of an optical element to leave room for its mount had an effect on the whole system, and though advertised, the generation of CAD files from the Zemax interface couldn't be straightforwardly integrated in the mechanical CAD (Figure 55 – left).

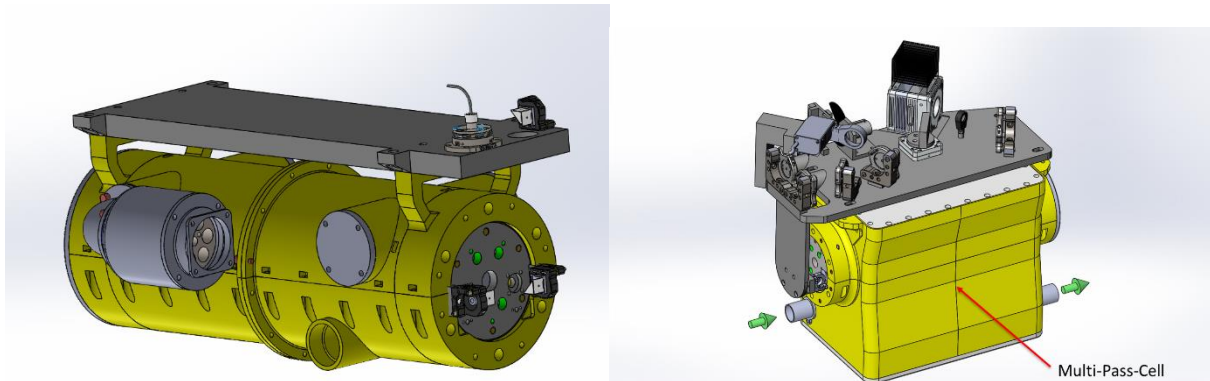


**Figure 53 : Evolution of the multipass cell design. (left) second design and (right) third design. This required drastic adaptation to the spectrometer interface design.**

The final prototype design is shown on Figure 54. The horizontal plate supports most of the spectrometer elements: the fiber collimator, followed by the chopper needed for signal modulation according to lock-in principle. Two flat mirrors allow for precisely align the beam toward a first OAP mirror. This mirror focuses the light in the perpendicular direction to the spectrometer baseplate. A 45° prism mirror then direct the light toward the entrance port of the MPC. After a certain number of reflections within the cell, a copy of the input beam exits the output port of the MPC. A 45° prism mirror directs it vertically towards a same model OAP mirror that collimates the beam on the spectrometer plane toward the diffraction grating. A third OAP mirror focusses the beam toward the NIT camera. A folding mirror has been added in order to reduce the overall size of the spectrometer. The cylindrical lens placed in front of the camera serves to spread the light vertically.



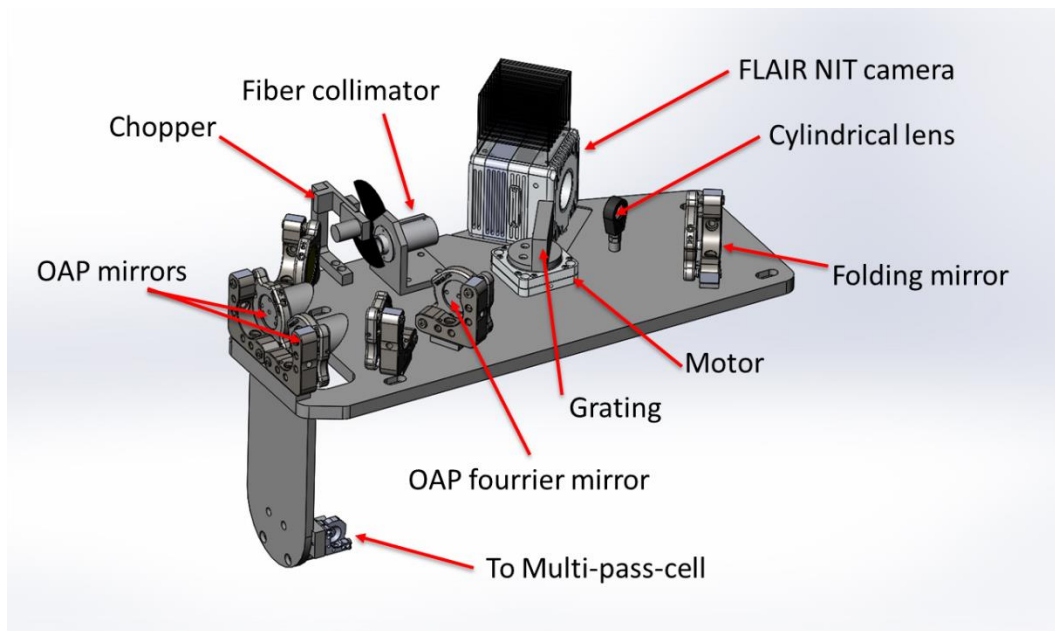


**Figure 54 : CAD of the single-grating based spectrometer prototype setup.**

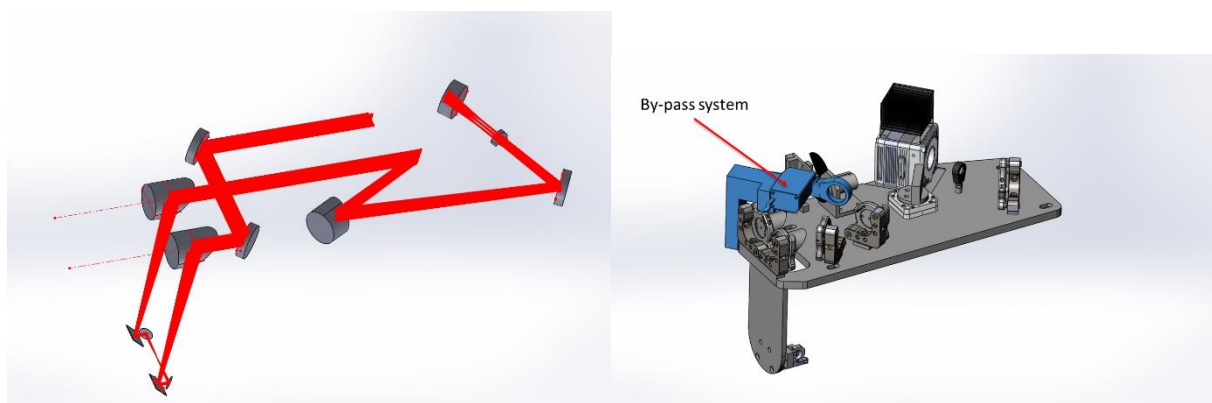


**Figure 55 : (left) Example of a Zemax export. The definition of the optics is not readily compatible with mechanical CAD. (right) Location of the flip-mirror based by-pass system.**

The prototype may require the acquisition of blank signals for self-recalibration purposes. As it is not convenient to flush the MPC with pure nitrogen on board the flying platform, an optical bypass system has been implemented on the spectrometer. Its physical location is shown in blue on Figure 55 (right), and in yellow on Figure 52 (left). It allows to direct the beam from the chopped supercontinuum directly towards the dispersion grating, without entering the MPC. It benefits from the fact that the beam exiting the MPC is a copy of the incoming beam. In-situ testing will be needed to validate the correct operation of this system. Alternatively, careful calibration of the system prior to and after the measurement campaign will have to be realized, as well as monitoring of the evolution of the water absorption signal in time compared with the data provided by the built-in humidity.

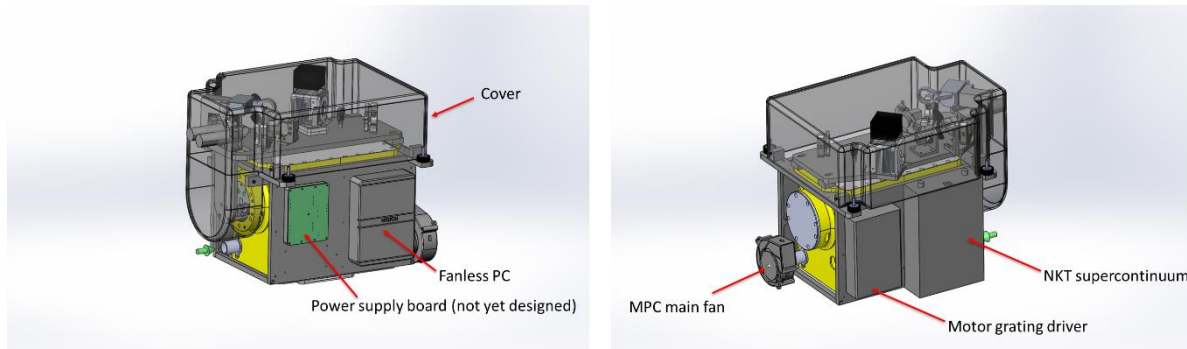


**Figure 56 : Design of the FLAIR full prototype with overall dimension  $45 \times 35 \times 35 \text{ cm}^3$ .**

Figure 56 illustrates the current design of the full prototype system. The optical part will be covered as a safety measure for the operators (laser exposure) and to avoid degradation of the optics. The NKT supercontinuum box, driver for the motor grating, control PC and power supply board are placed around the MPC. The current overall dimension stays below  $45 \times 35 \times 35 \text{ cm}^3$ , with a total weight estimated around 12.7 kg.

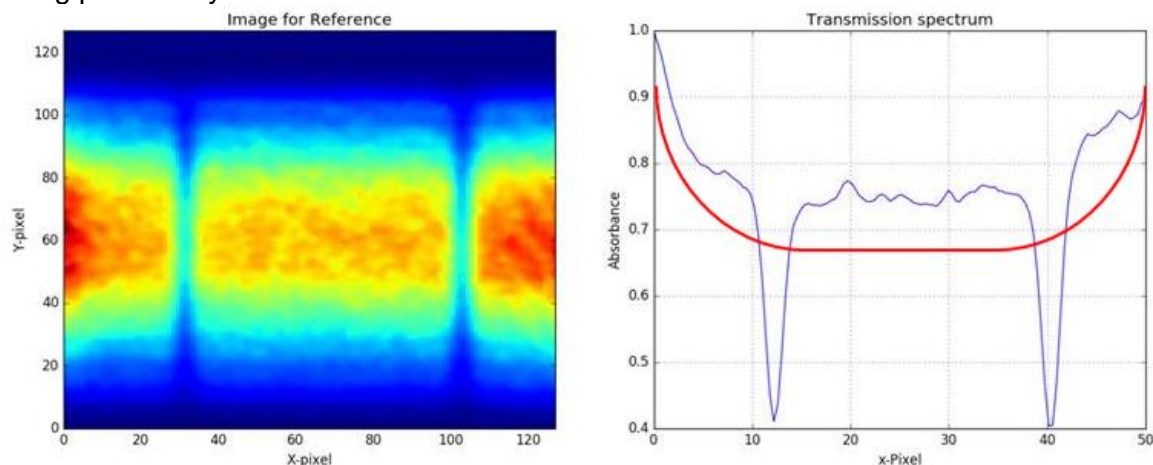
## 5.5 PbSe Camera

During the last 12 months NIT supported to CSEM in setting up the PbSe camera parameters and its integration in the FLAIR spectrometer.

NIT supported CSEM and contributed to optimize the following features related with the camera:

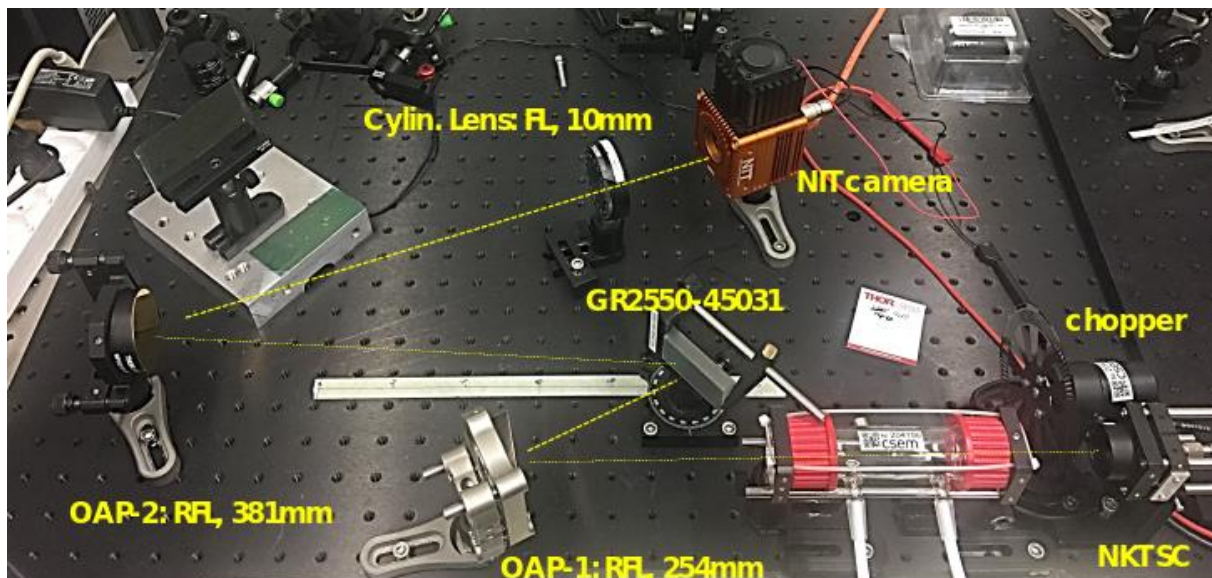
- 1) lockin algorithms implemented in the FLAIR acquisition system
- 2) No Uniformity Corrections measurements
- 3) Thermal management of the camera integrated in the system
- 4) Electronics adjustments for maximizing SNR
- 5) Mechanical parts for camera integration in spectrometer
- 6) Simulations of camera performances according FLAIR conditions

Figure 57 below shows the images obtained with the camera integrated in FLAIR spectrometer during preliminary trials.



**Figure 57 : (left) NIT camera acquisition and (right) corresponding column averaged spectrum. The red line illustrates the non-uniform gain pattern.**

Figure 58 below shows the camera integrated in the test bench at CSEM laboratories during commissioning and optimization phase..



**Figure 58 : Laboratory breadboard setup used during the optimisation phase.**

During the measurements, an unexpected U-shape gain response of the camera was observed. The individual pixel gain of the camera seems to be larger at the outer side of the 2D array of the camera than at the inner side of the array (See Figure 59). Such U-shape was constantly present while scanning the supercontinuum spectrum at the camera. Therefore, we believe that this might be attributed to the intrinsic response of the camera.

The unique function of the camera, so-called Non Uniform correction (NUC), was then applied to the camera, in order to correct such nonlinear response. But, this abnormal behaviour was not solved. However, it is important to mention that such nonlinear noise doesn't have any adverse impact on the performance, since the gas concentration computation relies on the baselining. The gas concentration is computed by comparing in-situ measurements to a reference measurement as baseline, which contains also such U-shape pattern.

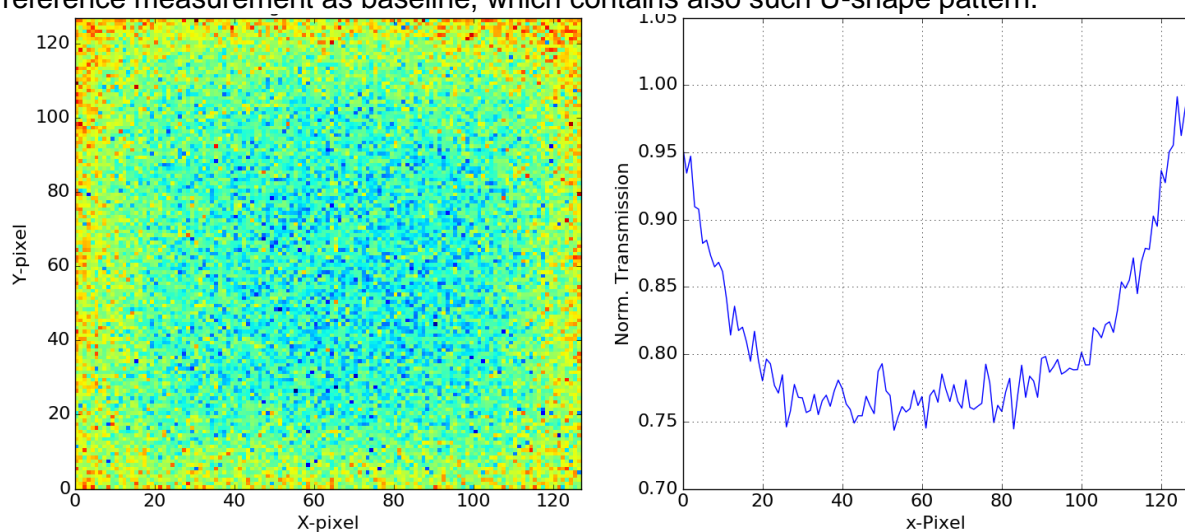


**Figure 59 : Camera image for a halogen lamp**



## 5.6 Data processing algorithm

The data processing algorithm, presented in section 5.6 of the second periodic technical report for VIPA based acquisition has been further developed. Some of its development, mainly concerning the extraction of linear absorption spectra from the 2D dispersed signal is now useless. However, an important portion concerning the demodulation of the lock-in signal could be reused. One of the improvement has been an adaptation of the demodulation lock-in frequency, which is robust against small frequency drifts, and dropping of camera frames.

Lock-in amplifier is utilised in the trace gas sensing system, in order to improve the SNR; hence, pushing the sensing sensitivity down to a few ppm for CH<sub>4</sub> monitoring. In general, any kind of sensing systems suffer from the detector and/or laser noise, which has usually Gaussian distribution. The advantage of the lock-in system is that such inevitable Gaussian noises can be totally eliminated, so that the SNR could be considerably enhanced.

An external mechanical chopper (See Figure 38) modulates the light intensity in time at a desired frequency, i.e., 117Hz. It means that all the information of the light is transferred from DC to the modulation lock-in frequency. So, simply by filtering in the lock-in frequency in electrical domain or by the numerical processing, which is called demodulation processing, the inherent system noise will be entirely removed.

Figure 60 illustrates the principle of the lock-in amplifier system. The chopper was operated at 117Hz and the camera acquisition speed was set to 1000fps (frame per second). Figure 60 (left\_bottom) shows the intensity profile in time at a pixel [Cartesian coordinates: 0,64] and Figure 60 (right\_bottom) shows the corresponding power spectrum of such intensity-modulated signal, simply by performing the Fourier Transform. As previously discussed, the signal information is transferred to a frequency at 117Hz, so in our case, a numerical narrow band-pass filter was used to accurately filter in only this frequency. After performing the demodulation process for all pixels, the demodulated image, as shown in Figure 60(left\_top) was obtained.

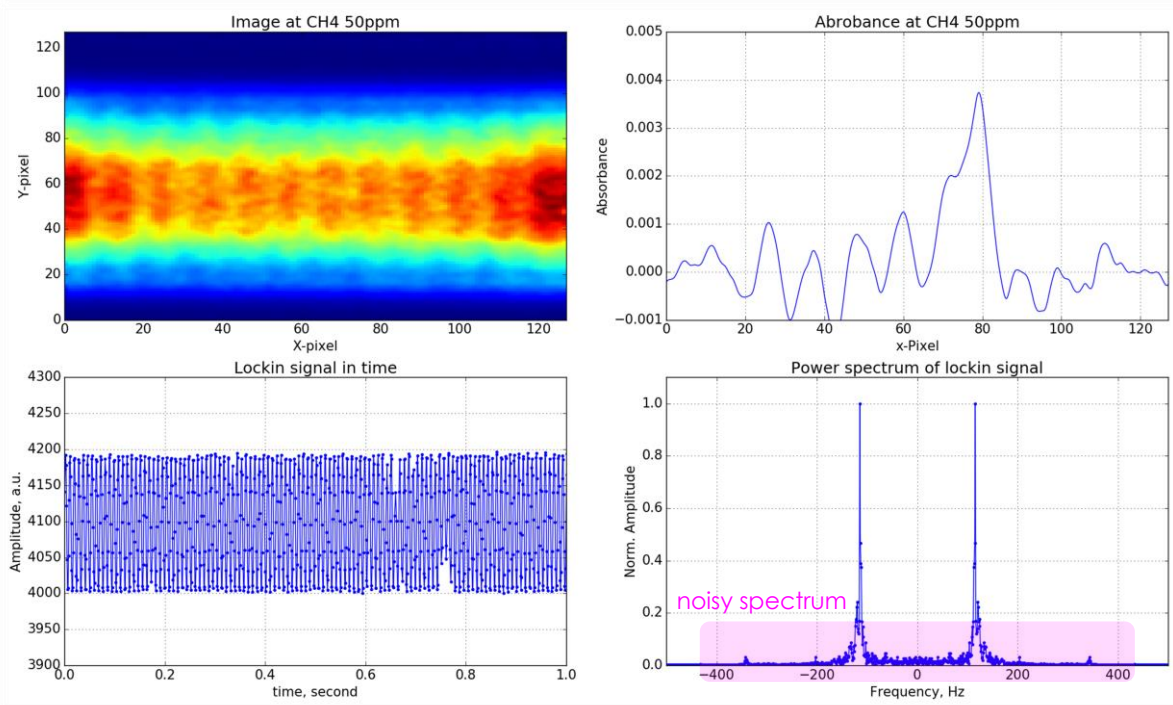


**Figure 60 : CH<sub>4</sub> 50ppm monitoring results, using a lock-in amplifier**

However, unfortunately, the unexpected noise generated by the nonlinear gain modulation of some pixels could not be entirely removed. The amplitude of such noise seems to be strong

and random, so that the power spectrum of this noise seems to be broadened over the vicinity of the lock-in frequency. As a result spurious peaks were imposed on the transmission spectrum, as shown in Figure 61(left). So, we applied a numerical median filter in the signal processing, which could sufficiently filter out the noise peaks, as shown in Figure 61(right).

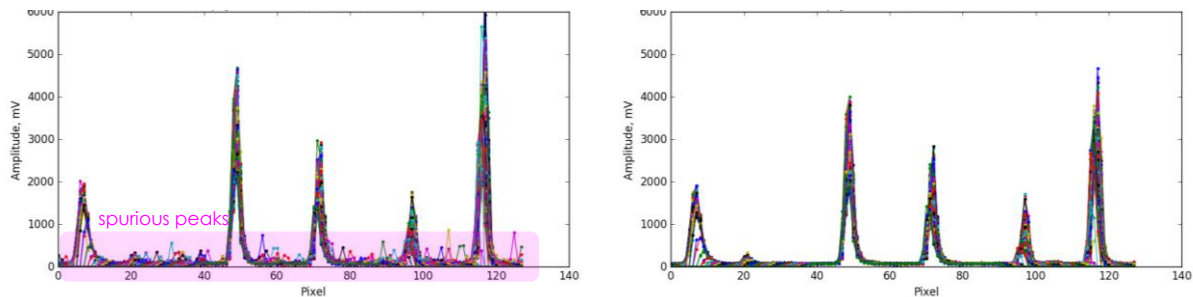


**Figure 61 : Demodulated signal, using echelle grating-based 2D spectroscopy**

Such demodulation processing was measured to be long, which acted as a practical limit, in terms of measurement speed. To reduce the measurement time, we run two processing in parallel: the camera acquisition and the data processing, as shown in Figure 62. Basically, two software tools: Labview and Python are used. Labview is connected to the NIT camera through TCP-IP protocol. In Labview, the camera acquisition parameters such as the frame speed and the sensing measurement speed can be set as desired.

Let us assume that 1000 fps and 1second measurement speed are set. It means that 1000 images will be required to provide a transmission profile. The camera will continuously acquire the image every 1ms due to the set parameter of 1000fps, and then each image will be saved in the PC RAM. Once 1000 images would be found, LabVIEW® will construct a 3D matrix (1000x128x128) to send it to Python through virtual TCP socket. Then, Python will perform the signal processing, mainly the demodulation processing and computing the transmission profile. Once it is done, Python will send its status to LabVIEW®, in order to monitor any possible error in the communication between the two software tools. This way the image acquisition and the signal processing could be performed in parallel and make it possible to achieve <1Hz measurement.

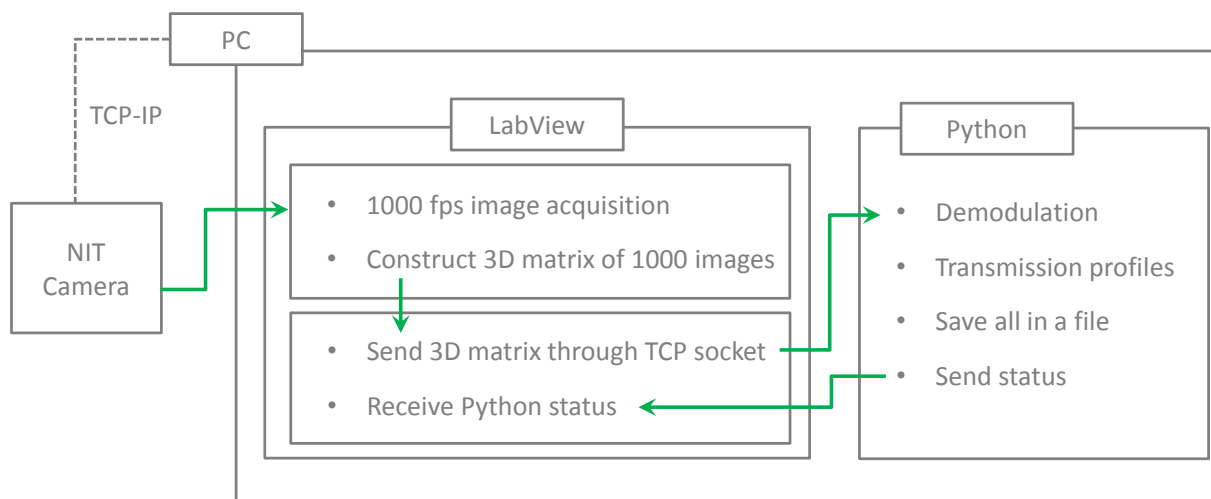


**Figure 62 : Simplified structure of gas sensing software algorithm**

## 5.7 Control electronics

The control electronic is split in two main contributors: the power supply, and the driving of various equipment with a LabVIEW® interface.



### 5.7.1 Control interface

So far, the acquisition and processing of the frames from the 2D NIT FLAIR camera into 1D absorption spectra has been finalized, as illustrated on Figure 62.

Currently, the supercontinuum is operated via a manual switch. However, preliminary tests on the 1<sup>st</sup> supercontinuum prototype provided by NKT demonstrated the possibility to switch the pump laser on and off through a simple set of command lines. Since the 2<sup>nd</sup> prototype relies on a similar pump laser, it is expected to work in a similar way.

The rotating platform of the grating has not been received yet, and suffers from a long lead time. The manufacturer provides LabVIEW® libraries for communication with their device.

The flip mirror is controlled through a trigger signal sent by the computer. As we just received the device, it has not yet been tested.

The multipass cell is controlled through its dedicated K92 control board (Figure 26), and CSEM relies on Senseair expertise to integrate a continuous data logging of the various MPC parameters, as well as a control of the temperature and fan speed in LabVIEW®.

### 5.7.2 Power distribution board

Some changes occurred since the previous periodic technical report, mainly concerning an effort to select 12 V equipment wherever possible in order to simplify the design of the power distribution board, the only exception being the supercontinuum source being operated at 24 V.

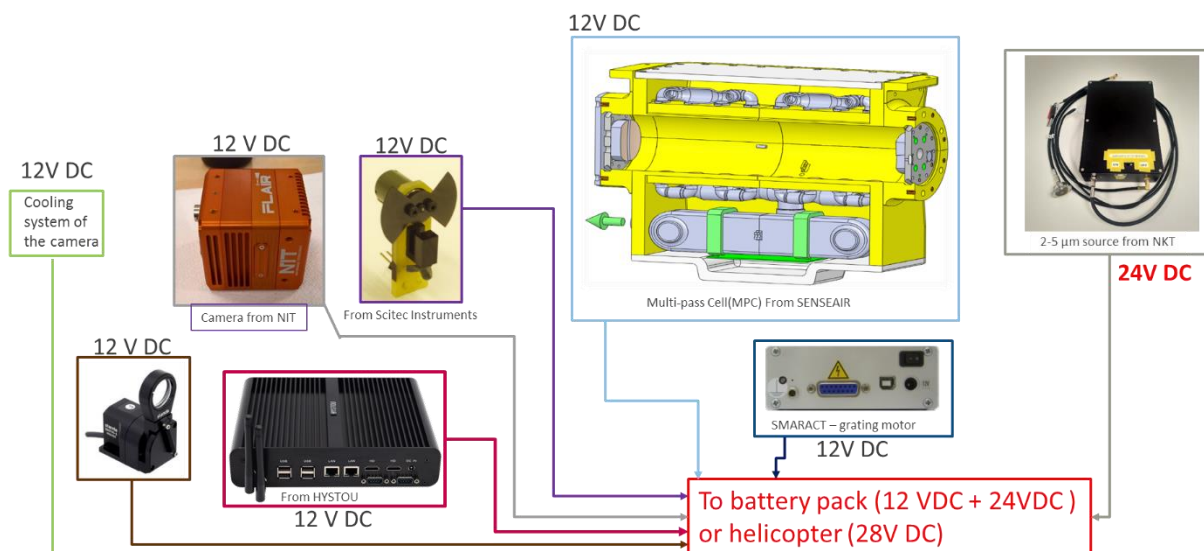


**Figure 63 : List of all the equipment requiring electrical power. The power is provided either through battery packs, or the flying platform.**

The power distribution board should accommodate 2 type of power sources. The helicopter turbines provides 28V, but the zeppelin does not have electrical powering capabilities. In this case, it is foreseen to use 12 V batteries packs. This is also compatible with the laboratory testing where adjustable power supplies are readily available.

**Table 4 : List of the powered equipment, with nominal voltage and power consumption.**

Equipment	Voltage (V)	Power (W)
Computer: HYSTOU P05B-i7-5500U	12	60.0
NIT Supercontinuum	24	16.8
NIT Camera	12	7.2
NIT Camera fan (alternative)	12	0.8
Chopper (7-15V)	12	7.2

Multi-pass cell total (incl. fan, heater, controller)	12	36.0
Grating motor controller	12	48.0
Mirror flip	12	8.4
Total		~185.0

The design of the control board has not been started within the reporting period, as the power consumption and voltage of the MPC has only been known recently.

CSEM expects to adapt a previous design in order to minimize the development risks. It is foreseen to group the different elements on separate switchable circuits in order to save power. One such group would contain the NIT Camera, fan, chopper and mirror flip, another will be dedicated to the MPC, a third one to the Grating motor controller. The PC will be always on, and the supercontinuum will be powered by a manual switch for safety reasons. The powering of those groups will be piloted by the board computer. It will allow to save power by switching unused elements off when not actively used (e.g. the rotating platform), or switching the MPC off during the short time needed to move the grating.

## 6 Airborne platform adaptation and sensor integration (WP5)

Work package 5, led by CSEM, includes the fitting of the **FLAIR** sensor to the airborne platform.

<b>Lead partner</b>	CSEM
<b>Contributing partners</b>	SA, NKT, NIT, CSEM

Airborne platform adaptation will be started once the final prototype is ready. Both subcontractor (helicopter, zeppelin) agreed on this, and are anyways waiting for the signature of their respective contract before adapting their platform.

CSEM makes sure that the prototype design is compatible with the requirement of both subcontractors, and information on both platforms have already been exchanged.

## 7 Validation and demonstration (WP6)

Work package 6, led by EMPA, includes the validation of the **FLAIR** integrated system and flight tests, test evaluation and recommendations.

<b>Lead partner</b>	EMPA
<b>Contributing partners</b>	RUN, SA, NKT, NIT, CSEM

EMPA has performed model experiments to plan the validation of the FLAIR instrument at Beromünster. The Beromünster tower has five inlet altitudes: 12, 45, 72, 132 and 212 m. For the validation, we will fly the FLAIR instrument on a suitable altitude comparable to the tower inlet height to measure concentrations of a gas released from a point source. Therefore, it is necessary to find the optimal weather conditions and distance from the point source, so the released gas reaches both, the tower inlet and the FLAIR instrument.

We used GRAL (Graz Lagrangian Model) on a 1x1 km domain with a flat topography (Figure 1). We considered different wind speeds (1, 2, 4 and 8 m/s), different insolation intervals (<20, 175-675 and 675-925 W/m<sup>2</sup>) and different distances from the gas release point (200, 300 and 400 m). In this setup, we used GRAL with constant wind speed in the horizontal and a logarithmic wind speed increase with altitude.

The model results (Figure 2) suggest that the most favorable weather conditions for the released gas to reach all inlet altitudes are high insolation ( $675\text{--}925\text{ W/m}^2$ ) with low wind speed ( $1\text{ m/s}$ ). These weather conditions are typical for summer days with clear sky, when the atmosphere is unstable. Source distance of  $400\text{ m}$  proved to be most effective in reaching all inlet altitudes. If we use one bottle of methane as a point source (with constant gas release of  $50\text{ l/min}$ ), the model predicts an increase methane mixing ratio of  $1\text{--}10\text{ ppbv}$  at the tower's  $72\text{ m}$  inlet. This signal can be linearly amplified adding more gas bottles.



**Figure 1.** GRAL model domain. Yellow pin marks the Beromünster tower, while the red X's mark considered placements of the point gas source.

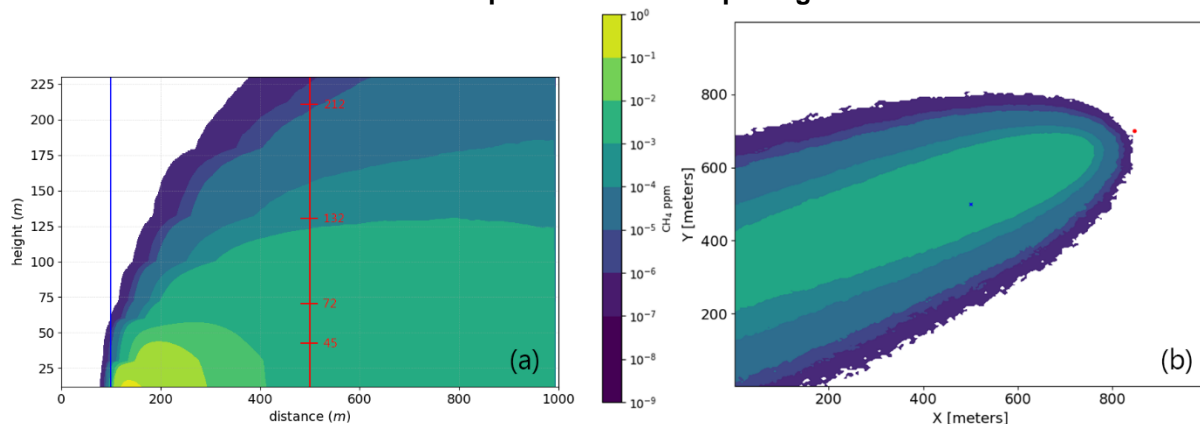


**Figure 2.** GRAL model results. (a) vertical and (b) horizontal (at  $72\text{ m}$  altitude) cross-section of modeled gas. Vertical blue line represents placement of the gas source and the vertical red line marks the position of the tower with altitudes of the inlets.

## 8 Other

### 8.1 Dissemination

CSEM presented the work on the VIPA based spectrometer, with an introduction to the FLAIR project, at

- CLEO Europe 2019 in Munich: J. Gouman et al, *Compact, UAV compatible 2D Spectrometer for multi-species atmospheric gas analysis*
- OSA Laser Congress 2019 in Vienna: S. Chin et al, *Compact UAV compatible broadband 2D Spectrometer for multi-species atmospheric gas analysis.*

NIT has participated as exhibitor in the following trade shows and Conferences:

- Photonics West 2019, 2<sup>nd</sup> – 9<sup>th</sup> February San Francisco.
- Laser World of Photonics 2019, 24<sup>th</sup> – 27<sup>th</sup> June, Munich



Figure 64 : NIT conference boot advertising the TACHYON 16k Camera and the FLAIR project.